Materials Advances

ROYAL SOCIETY OF CHEMISTRY

REVIEW

View Article Online
View Journal | View Issue

Open Access Article. Published on 31 ožujka 2023. Downloaded on 8.8.2024. 13:17:39.
This article is licensed under a Creative Commons Attribution-NonCommercial 3.0 Unported Licence.

Cite this: *Mater. Adv.*, 2023, 4, 1850

Enhancing memristor fundamentals through instrumental characterization and understanding reliability issues

Fei Qin,[a] Yuxuan Zhang,[a] Han Wook Song[b] and Sunghwan Lee *[a]

Received 13th February 2023,
Accepted 23rd March 2023

DOI: 10.1039/d3ma00069a

rsc.li/materials-advances

Memristors, a two-terminal device, have a resistance that can be changed and retained in two or more different states when subjected to electrical stresses. This unique function makes memristors now an attractive area of research for next-generation electronic devices such as memory and advanced computation. However, credible characterization methods for memristors are not fully established yet to understand fundamental working mechanisms and objectively evaluate figures of merit performance. This review encompasses various characterization methods from materials to electrical characteristics to identify the fundamentals of memristor operations. Meanwhile, large performance variation is the main bottleneck hindering the adoption of this class of devices in practical applications. Thus, the second part of this article focuses on the types of variation and other reliability issues of memristors. Possible strategies to enhance reliability are suggested as well. Topics covered in this review on memristors' characterization techniques and reliability are of significant relevance to many studies that seek to advance the state of the art in electronic devices and systems towards neuromorphic computing.

1. Introduction

A memristor was proposed as a two-terminal electronic device by Leon Chua in 1971.[1] It is a non-linear passive circuit element that can exhibit different resistance states, depending on the history of the voltage applied across its terminals. The first experimental demonstration of a memristor device was reported in 2008 by a research group led by R. Stanley Williams at Hewlett-Packard (HP) Laboratories.[2–5] They used a thin film of titanium dioxide to create a memristor that exhibited the expected non-linear current–voltage characteristics and hysteresis behavior. After HP's experimental demonstration, several other teams around the world made significant efforts to independently reproduce the memristor behavior using different materials such as TaO_x, HfO_x, and InGaZnO.[6–21] Then, research in memristors has gained significant attention due

[a] *School of Engineering Technology, Purdue University, West Lafayette, IN 47907, USA. E-mail: sunghlee@purdue.edu*
[b] *Center for Mass and Related Quantities, Korea Research Institute of Standard and Science, Daejeon 34113, Republic of Korea*

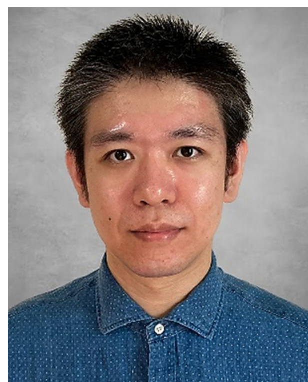

Fei Qin

Fei Qin is currently a PhD student in the School of Engineering Technology at Purdue University, under the supervision of Professor Sunghwan Lee. He received his Bachelor's degree in Applied Physics from Xi'an Jiaotong University and Master's degree in Physics from Temple University. His research primarily focuses on the design and optimization of memristors towards neuromorphic computing.

Yuxuan Zhang

Yuxuan Zhang received his Bachelor's and Master's degrees in Materials Science and Engineering from the University of Science and Technology Beijing in 2016 and 2019 respectively. He is currently a PhD student at the School of Engineering Technology at Purdue University, under the supervision of Professor Sunghwan Lee. His research primarily focuses on the design and optimization of electrode materials for high energy density Li-ion batteries.

 © 2023 The Author(s). Published by the Royal Society of Chemistry

Open Access Article. Published on 31 ožujka 2023. Downloaded on 8.8.2024. 13:17:39.
This article is licensed under a Creative Commons Attribution-NonCommercial 3.0 Unported Licence.

to the potential applications in various fields such as memory with a particular focus on higher-performance solid-state device technologies leveraging its binary switching behavior.[22,23]

More recently, the synaptic switching behavior of memristors has been attracting increasing attention due to its potential applications in a variety of neural networks.[24–26] Besides binary switching, the memristor's resistance can change continuously over a wide range of values, depending on the history of the pulse voltage applied across their terminals. This tunable multiple resistance level ability is crucial for neuromorphic computing because it can be used to adjust the weight of the connection between artificial neurons in a more precise and continuous way, to mimic the behavior of real synapses.[27,28] Thus, memristors have been proposed as a key building block on the roadmap of neuromorphic computing and engineering.[29]

It is essential to understand the switching mechanisms of the memristor and measure the performance of the memristor by employing suitable characterization methods, which may require the exquisite design of testbeds and the non-trivial handling of materials and devices. From a material science of view, state-of-the-art, such as, transmission electron microscopy (TEM), X-ray photoelectron spectroscopy (XPS), and atomic force microscopy (AFM) are useful techniques to map and visualize the switching mechanisms and characterize the materials from each layer which in turn can provide experimental evidence of the switching behavior and insight for material selection and structure design. The mechanism for a memristor, in short, involves the movement of ions through a switching layer, causing a formation of conductive filament(s) (CFs). And TEM is a great technique to visualize this filament evolution, in the either planar or vertical structure of memristors. Also, the composition of the filament can be identified by further analysis with assistance from X-ray energy dispersive spectroscopy and electron diffraction. The chemical composition of the switching layer is a governing factor of the memristor performance. Especially, the switching behaviors of the valence change mechanism (VCM)-based memristors are driven by the change of the oxygen vacancy. With XPS characterization, one can examine the oxygen vacancy concentration of the fabricated switching layer, and then fine-tune and optimize the composition for better performance. The morphology of the memristor during the electrical stress is crucial information as well since it can degrade its performance. The surface distortions following electroforming and subsequent cycling between resistance states have been observed by XPS.

The electrical measurements are covered in this review, from DC sweeping to pulse measurements. DC sweeping is served as a starting point of the electrical characterization of a memristor. The memristive switching can be identified and endurance performance can be extracted. For fast testing and neuromorphic applications, pulse measurements are required essentially, thus, two pulse train profiles are selected and compared in this review for endurance and linearity characteristics. Advanced characterization of image processing which is to identify analog tuning accuracy is included as well. From an electro-chemistry perspective, cyclic voltammetry (CV) and electrochemical impedance spectroscopy (EIS) are also discussed for investigation on redox processes occurring prior to and during the switching events, respectively. This can provide valuable information for material selection and switching mechanisms. Detailed strategies and key achievements of each characterization method will be comprehensively discussed. Extensive studies have been reported on both single memristor devices and circuited devices with required structures such as crossbar arrays for practical applications such as neuromorphic computing hardware and random number generator.[30,31] However, reliability, for example, the retention and endurance behavior of the memristors, has remained one of the fatal

Han Wook Song

Dr Han Wook Song is a Principal Research Scientist at Korea Research Institute of Standards and Science (KRISS) since 2006. He obtained his PhD degree in Materials Science and Engineering from KAIST in 2002. His research background includes the fabrication and characterization of thin film materials, especially piezoelectric materials for energy and sensing. His current research focuses on the establishment of national vacuum standards such as a quantum-based redefinition of vacuum. To this end, he evaluates and standardizes the pressure of objects through novel refractive index-based approaches.

Sunghwan Lee

Dr Sunghwan Lee is an Assistant Professor of Engineering Technology at Purdue University. He received his PhD degree in Materials Science and Engineering from Brown University in 2013. He completed postdoc training at MIT and Harvard University from 2013 to 2015. His current research pertains to the design and discovery of functional thin film materials to fundamentally understand the process–structure–property relationships. He is particularly interested in the engineering of defect structures, interfacial properties, and nanostructured materials with new functionalities for energy storage and conversion, transparent and flexible electronics, and sensing applications.

© 2023 The Author(s). Published by the Royal Society of Chemistry

Open Access Article. Published on 31 ožujka 2023. Downloaded on 8.8.2024. 13:17:39.
This article is licensed under a Creative Commons Attribution-NonCommercial 3.0 Unported Licence.

weaknesses which hinder their industrial adoptions in such applications. It is urgent to identify and categorize the metrics, symptoms, and solutions of memristors' reliability issues. Thus, the second major part of this review is focused on typical reliability issues: cycling endurance, variation, retention, and nonlinearity. Less cycling endurance and retention directly shorten the lifetime of the functional memristors since the conductance levels are not distinguished anymore due to device degradation or failure. And larger order of variation, nonlinearity, and asymmetry cause accuracy loss during the processing of memristors' operations. To identify and address these critical issues, possible mitigating strategies are covered and discussed. Density functional theory (DFT) and molecular dynamics (MD) calculations provide atomic- or molecular-level information that is not typically available from macroscale characterizations for examining the formation energy of defects, the energy barriers associated with ion migration, and the atomic-level dynamics of resistive switching. These calculations serve as valuable complements to instrumental characterizations.

To date, numerous review articles have been available, however, most of them are mainly review memristors by different materials selection (*e.g.*, HfO_x, TaO_x *etc.*) or fascinating demonstrations of novel neuromorphic applications. It is rare to find reviews that focus both on characterization methods for a fundamental understanding of memristors' behavior and directly intend to tackle one of the most major issues – reliability. Thus, we provide this review and further aim to fill the gap in this field. Since the memristors keep attracting attention, this review can pave the way and clean the blurry area for researchers and also be beneficial to the whole community to accelerate the development of memristors towards practical applications such as neuromorphic computing.

Part I. Characterizations for memristors

2. Transmission electron microscopy (TEM)

Transmission electron microscopy (TEM) is widely employed to obtain plan-view or cross-sectional images, featuring high-resolution microstructures, crystallographic information, and chemical elemental mapping often together with EDX.[32–39] In addition, a wide range of *in situ* investigation capabilities are available in vacuum or environmental conditions, from which time-resolved evolution of materials structure and response to the stimuli such as temperature and bias can be recorded.[40–42] Therefore, as a characterization approach to identifying materials and device behaviors for memristors, TEM is highly beneficial in not only *ex situ* structure analysis but also in visualizing the dynamic evolution of filaments *in situ*.[43]

Fig. 1a and c show schematic illustrations of memristors with top electrodes (TE) and crossbar arrays, and Fig. 1b and d demonstrate corresponding cross sectional TEM images of these devices.[21,44] Each layer of these memristors were clearly inspected and the uniform switching layers were identified. High-resolution (HR) TEM images associated with fast-Fourier-transform (FFT) diffraction patterns and EDX elemental analysis are instrumental to visualize the dynamic evolution process of conduction filament, through which the morphology, defect generation/annihilation, and composition are mapped *in situ* as well as *ex situ*. These capabilities of TEM have been leveraged to fundamentally understand and establish the switching mechanisms of memristors with vertical and planar configurations.[32–37,45,46] Yang *et al.* contrived a SiO_2-based planar memristor for TEM investigations where a novel TEM specimen (inset schematic of Fig. 1e) was devised with a $\sim$15 nm (lateral length) SiO_2 switching layer sputtered on a 15 nm-thick SiN_x low-stress membrane with an active electrode of Ag and an inert electrode of Pt.[46] The thin SiN_x membrane was employed to achieve a lower (brighter) background so that a higher contrast can be produced during TEM measurements. It should be noted that the planar design (memristor/TEM specimen) is unique in that the lateral structure can image the entire filaments, which is not available in vertical configurations and, hence, enables direct investigation of the evolution of filaments. In this *ex situ* measurements, the memristor was switched on and off in a separate controlled environment (*i.e.*, before loading into the TEM chamber) and only exposed to high energy electrons during the imaging process, minimizing possible damages to the materials and device. Fig. 1e shows a plan-view TEM image of a pristine device, exhibiting the initial high resistance state (*i.e.*, no filament formed) of the memristor. After applying a positive bias on the Ag electrode, filaments that completely and incompletely connect the two electrodes are recognized in Fig. 1f. With associated FFT analysis (Fig. 1h), the composition of the filaments was confirmed as Ag. Then, after a RESET process, both complete and incomplete filaments were dissolved from the switching layer/inert electrode (*i.e.*, SiO_2/Pt) interface, which is shown in Fig. 1g. The TEM images obtained from the main memristor states (initial, SET, RESET) convincingly suggest operation fundamentals of particularly ECM memristors, such as a self-limiting formation of filaments,[47] which describes once a dominate filament is established, it reduces the electric field across the switching layer, in turn, restrains further formation of filaments, and the redox process of the EMC ions (*i.e.*, Ag cations) at the inert electrode.[48,49]

TEM examinations from vertically stacked memristors were also demonstrated, by which the formation/rupture of the conduction filament was imaged from more typical device structures. Fig. 1i shows a cross-sectional TEM image of Ta_2O_5-based memristors individualized by applying focused ion beam (FIB) to vertically deposited Pt/Ta_2O_5/Ru layers.[50] The thickness of sputtered switching layer Ta_2O_5 was only 5 nm to make it electron transparent which is beneficial for TEM observation. The bottom Ru layer is continuous (not divided by FIB), thus, bottom electrodes of all nanopillar memristors by FIB are connected to each other and also connected to the bottom contact for grounding, which is

 © 2023 The Author(s). Published by the Royal Society of Chemistry

Open Access Article. Published on 31 ožujka 2023. Downloaded on 8.8.2024. 13:17:39.
This article is licensed under a Creative Commons Attribution-NonCommercial 3.0 Unported Licence.

Fig. 1 A demonstration of a typical two-terminal memristor: (a) schematic of typical vertical configuration memristors with top and bottom electrodes where the top electrodes define the memristor sizes and (b) its associated cross-sectional TEM image, presenting the device structure of ITO bottom electrode, IGZO switching layer, and ITO top electrode. Reproduced with permission from ref. 21. Copyright 2022, John Wiley and Sons, an example of a memristive crossbar: (c) schematic of crossbar arrays of memristors and (d) its cross-sectional TEM image, showing the vertical structure of a single memristor (Ti/PdSe/Au) from the arrays. Reproduced with permission from ref. 44. Copyright 2021, Springer Nature, observation of conductive filaments in a planar memristor by TEM: a TEM image of a pristine SiO_2-based planar memristor. (f) After the first-time turn-on process, a TEM image was captured to visualize the complete and incomplete filaments. (g) After RESET process, the TEM image shows that all filaments were dissolved. (h) FFT results of the HRTEM image of an Ag nanoparticle in the filament of the switching layer, which indicates Ag (111) was identified. Reproduced with permission from ref. 46. Copyright 2012, Springer Nature, TEM examination on conductive filaments evolution in a vertical memristor: (i) bright-field TEM image of nanopillar shape samples for TEM imaging by ion-beam milling. (j) Setup to apply bias through a probe tip on the Pt(top)/Ta_2O_5/Ru(bottom) memristor for *in situ* TEM investigation. Cross-sectional *in situ* TEM images of (k) the pristine state (HRS), (l) after SET state (LRS) where two conductive filaments are observed, and (m) after RESET, back to HRS. Reproduced with permission from ref. 50. Copyright 2020, John Wiley and Sons.

highlighted with an empty red square in Fig. 1j. And the examination sample was loaded to a nano-biasing holder. To make a good contact between the probe and carbon-coated Pt top electrode, a sharpen and flexible gold tip was employed. A clear sandwich structure with a uniform 5 nm Ta_2O_5 switching layer was identified in the Fig. 1k for the initial state of the device. After a SET process, *i.e.*, a negative bias was applied on the Pt through the Au tip, two distinguishable Ru filaments were able to be observed in Fig. 1l. The Ru filaments yielded by the migration and accumulation of Ru were identified with *ex situ* EDX analysis, indicating a low resistance state established. Afterwards, with a RESET process by applying a positive through the Au tip, the Ru filaments were dissolved and generated a high resistance state which is presented in Fig. 1m.

From these studies of *in situ* and *ex situ* TEM investigations, the fundamental memristor switching mechanisms involving the formation and rupture of conduction filaments were visually identified at the nanoscale. Therefore, TEM is a powerful technique to characterize the device structure, more importantly, the morphology and composition of conductive

Open Access Article. Published on 31 ožujka 2023. Downloaded on 8.8.2024. 13:17:39.
This article is licensed under a Creative Commons Attribution-NonCommercial 3.0 Unported Licence.

filaments evolution which can reveal the switching mechanism definitively.

3. X-Ray photoelectron spectroscopy (XPS)

X-Ray photoelectron spectroscopy (XPS) offers a high-resolution identification of chemical environment of elements within a material, valence states, and electronic structures.[51,52] Due to these capabilities, XPS has been utilized in memristor applications to identify the chemical composition, doping states and functional bonding of the memristor components (*i.e.*, switching layer and electrodes).[53–63] Therefore, XPS is instrumental to analyze the major factors which control the evolution of the filaments and hence enhance the fundamentals of the switching mechanisms.

With a TaO_x-based memristive crossbar, Kim *et al.* demonstrated a functionally complete three-valued Łukasiewicz logic system, which describes a multivalued logic for enhancing the computing efficiency by reducing the data size.[64] At the single device level, the oxygen content in each oxide layer of a bilayered tantalum oxide-based memristor was modulated by adjusting the partial pressure of O_2 during the deposition. Through XPS, the valence state of Ta and the oxygen deficiency were identified to understand their effect of the chemical environment on the memristor behavior. The structure of the bilayered memristor is schematically shown in Fig. 2a where the '$x-$' and '$x+$' represent that TaO_{x-} is more oxygen-deficient than TaO_{x+}. And this oxygen content differentiation was confirmed by the high resolution (HR) XPS analysis of the Ta 4f spectra in Fig. 2b, indicating both layers were oxygen-deficient and quantitatively $x- = \approx 1.6$ and $x+ = \approx 1.9$, in reference to the stoichiometric phase, Ta_2O_5. The bottom table in Fig. 2b summarizes the atomic percentage of each valence state of Ta in the bilayers. The O 1s HR spectra for both layers were examined and depicted in Fig. 2c. The blue peak, which is located at 530 eV and referred to as O_I, and the green peak, which is located at 531 eV and referred to as O_{II}, are associated with the bonding of Ta and O in a stoichiometric Ta_2O_5 and oxygen-deficient tantalum oxide, respectively. The ratio of the area of O_I (blue) to O_{II} (green) is 3.57 in TaO_{x-} and 5.0 in $TaO_{x\pm}$, validating that TaO_{x-} is more oxygen-deficient, aligning with the results of the Ta 4f spectra. With the optimized oxygen content, the bilayered tantalum oxide-based memristor operates in three distinct states: LRS, HRS, and an intermediate resistance state (IRS). Fig. 2d shows the retention characteristics for these states, and they are stable enough to demonstrate the potential application

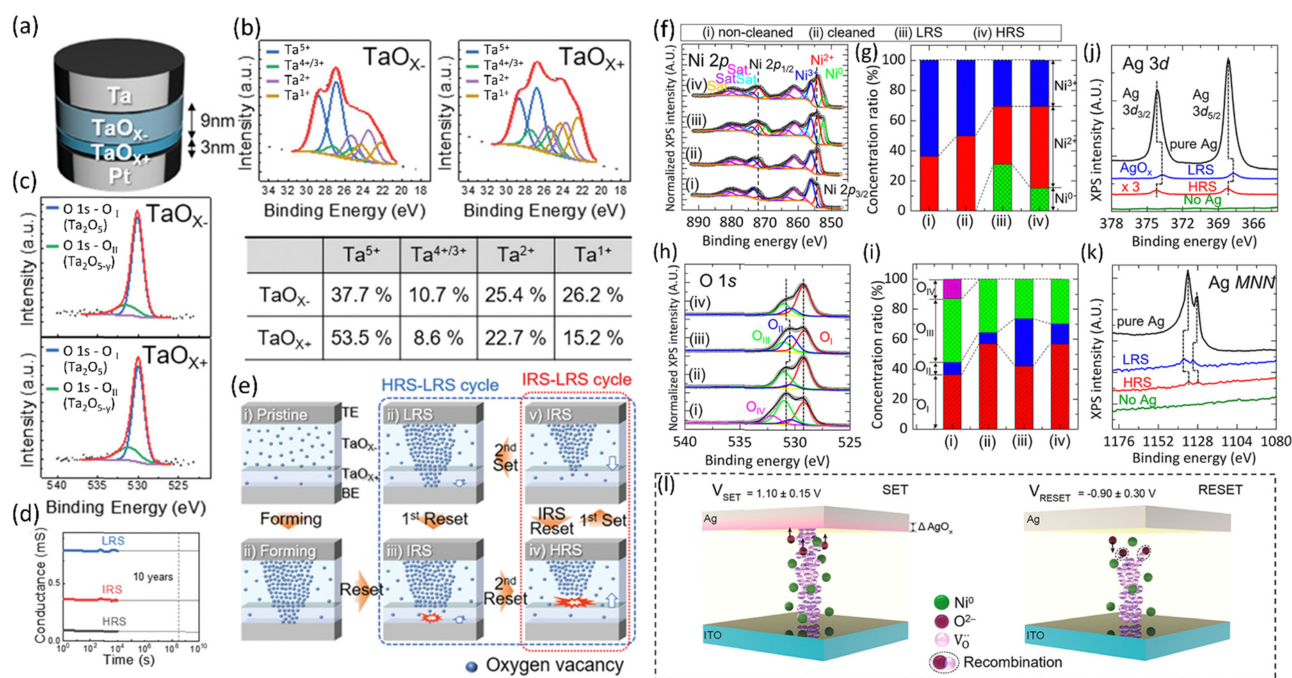

	Ta5+	Ta4+/3+	Ta2+	Ta1+
TaOx-	37.7 %	10.7 %	25.4 %	26.2 %
TaOx+	53.5 %	8.6 %	22.7 %	15.2 %

Fig. 2 XPS analyses for optimizing compositions of the switching layer and identifying the switching mechanisms. Bilayer TaO_x-based memristors: (a) the structure of a bilayer tantalum oxide memristor. (b) Core-level HR Ta 4f XPS with peak fittings of each tantalum oxide layer and associated atomic percentage. The table summarizes the atomic percentage of each peak estimated from the HR XPS analyses. (c) XPS O 1s peak fittings of tantalum oxide layers. (d) Retention measurements at the three resistance states (R_{LRS}, R_{IRS}, and R_{HRS}) of the bilayer tantalum oxide memristor (e) schematic illustration of the switching mechanism of the bilayer tantalum oxide-based memristor, describing LRS, HRS and IRS. Reproduced with permission from ref. 64. Copyright 2021, published by John Wiley and Sons. This is an open access article distributed under the terms of the Creative Commons CC BY license, and NiO_x-based memristor: XPS spectra of (f) Ni 2p core level and (h) O 1s core level and the associated valence-state concentration ratio in (g and i), respectively. (j) Ag 3d core level XPS spectra of pure Ag (TE), both LRS and HRS states with a control condition (*i.e.*, no Ag). (k) Associated Auger spectra of Ag MNN. (l) Proposed switching mechanism of NiO_x-based memristor based on the XPS analysis. Reproduced with permission from ref. 39. Copyright 2022, American Chemical Society.

Open Access Article. Published on 31 ožujka 2023. Downloaded on 8.8.2024. 13:17:39.
This article is licensed under a Creative Commons Attribution-NonCommercial 3.0 Unported Licence.

for a logic system representing ternary states. The switching mechanism from oxygen concentration-modulated TaO_{x-}/TaO_{x+} was proposed as in Fig. 2e where blue dots represent oxygen vacancies and each state with oxygen vacancy distribution is illustrated. Comparing with TaO_{x+}, the oxygen-vacancy concentration is higher in the TaO_{x-} layer in the pristine state. The first SET (*i.e.*, forming) process yielded a conical shape conductive filament and it has wider width in the TaO_{x-}, and only the thinner (weaker) filament in TaO_{x+} was dissolved during the first RESET process. With the second RESET process, the wider (stronger) filament in TaO_{x-} was destroyed as well, leading to HRS. Then, only TaO_{x-} filament was recovered by a SET process due to a larger oxygen vacancy concentration in TaO_{x-} layer, creating the IRS. An additional SET is needed to extend the filament to TaO_{x+} for LRS.

XPS may enable one to investigate chemical content variation for each switching stage, through which the switching mechanism of a memristor can be established. Park *et al.* reported such an investigation on NiO_x-based memristors.[39] XPS analyses were carried out for the four following cases: (i) non-cleaned NiO_x, (ii) cleaned (by ion beam) NiO_x, (iii) NiO_x at LRS, and (iv) NiO_x at HRS. Fig. 2f exhibits the Ni 2p core levels XPS data for the four cases, where green Ni^0 peaks are only observable in the case (iii) LRS and (iv) HRS, indicating a shift in the Ni 2p peaks. Fig. 2g compares the concentration ratios of Ni^{3+}, Ni^{2+}, and Ni^0 in the four cases. And it shows that a significant change in concentration ratios of Ni^{2+} and Ni^0 occurred in (iii) LRS and (iv) HRS, whereas Ni^{3+} remained stable due to a stronger Ni^{3+}–O bond. Thus, oxygen vacancies were formed around Ni^{2+} ions in LRS. O 1s core levels XPS spectra for four cases are plotted in Fig. 2h. The pink O_{IV} peak at 532.4 eV indicates the presence of weak binding and/or interstitial oxygen and surface hydroxyl groups, *i.e.*, NiO(OH), Ni^{3+} state, and O_{IV} peak can be perceived only in case (i) pristine NiO_x. The NiO_x film was cleaned in case (ii) with an Ar^+ ion beam to remove chemical adsorption on the NiO_x surface, resulting in a removal of the O_{IV} peak. Peaks of O_I, and O_{III} are related to oxygen lattice, oxygen vacancy, and non-lattice, respectively. According to Fig. 2i, from (iii) LRS to (iv) HRS, the oxygen-vacancy (O_{II}) concentration decreased from 31.7% to 13.5%, while O_{III} was barely changed, similarly due to the strong bonding of Ni^{3+}–O. In case (iv) HRS, the O^{2-} ions repopulate the original lattice position of the NiO_x, leading to a decrease in oxygen vacancy. In contrast, in case (iii) LRS, Ni^{2+} is reduced to Ni^0. The XPS analysis was used to estimate the Ni and O composition ratios for cases (ii) to (iv). In case (ii), the Ni and O composition ratio was determined to be 1 : 1.3 without the presence of Ni^0. After the forming process, this ratio shifted to 1 : 0.9 in case (iii) LRS and 1 : 1.2 in case (iv) HRS when Ni^0 was present. This quantitative analysis implies that the digital bipolar switching behavior of the NiO_x-based memristor is related to the valence change mechanism (VCM), which is influenced by changes in the oxygen vacancy within the NiO_x layer. With further analyses of Ag $3d_{3/2}$ and Ag $3d_{5/2}$ core levels XPS spectra in Fig. 2j and associated Auger spectra of Ag MNN in Fig. 2k, the authors claimed the bipolar switching behavior arises from various electrochemical reactions at the Ag/NiO_x interface, involving Ag and AgO_x, and within the NiO_x layer, involving Ni^{2+} and Ni. The switching mechanism of the Ag/NiO_x/ITO memristor can be demonstrated based on the XPS analysis, as depicted in Fig. 2l. When SET voltage is applied to the Ag top electrode, the O^{2-} ions from the NiO_x layer are able to easily move into the Ag electrode, which results in the separation of the O^{2-} ions from the oxygen lattice sites, or the drift of oxygen vacancy. The partial O^{2-} ions from NiO_x then gather at the Ag/NiO_x interface, leading to the formation of AgO_x (left side of Fig. 2l). In the NiO_x layer, the conductive filament can be established between Ag/AgO_x and ITO, switching the device to its LRS. On the other hand, when a RESET voltage is applied to the Ag top electrode, the O^{2-} ions from AgO_x are replenished back to the NiO_x layer, partially neutralizing and recombining with oxygen vacancy (right side of Fig. 2l). This process can lead to the partial rupturing of the filament near the Ag top electrode, switching the device to its HRS.

4. Atomic force microscopy (AFM)

Atomic force microscopy (AFM) is a technique used to measure not only the typical surface topography and mechanical properties but also electrical response, electronic structures (*e.g.*, work function), and electrochemical behavior of materials at the nanoscale.[65–73] It works by scanning a very sharp probe over the surface of a sample, and measuring the various signals between the probe and the surface. By plotting these signals as a function of the probe's position, an AFM can produce a detailed map of such informative properties to understand the nature of materials.[74]

In addition to these various capabilities, it is further promising for memristor characterizations that AFM can identify the changes that occurred in these properties during the operation of the memristor. This information can be used to understand the mechanisms by which memristors function, and to optimize their performance.[75,76] For example, AFM can be used to measure the resistance of a memristor as a function of applied bias through, known as conductive AFM (C-AFM or current mapping), which can provide insights into the mechanisms underlying the device's resistive switching behavior.[77] AFM can also identify the effect of the surface roughness and roughness distribution of the materials on the memristor performance.[78]

Sun *et al.* used the current mapping method on $CH_3NH_3PbI_3$ ($MAPbI_3$)-based memristors to investigate the switching mechanism.[79] The tip of C-AFM was coated with Pt and served as a grounded top electrode, and Fluorine-doped Tin Oxide (FTO) is the bottom electrode where a bias voltage is applied (*i.e.*, Pt/$MAPbI_3$/FTO structure). The measurement is schematically described in Fig. 3a. The large bias voltage is applied to the upper part of the sample only. After the upper scanning, a full scan is carried out on the whole area of the sample with a small voltage, basically this is a read process. Fig. 3b shows the current mapping for a −8 V upper scanning and Fig. 3c presents a 0.5 V full read mapping. At another area with the same

Open Access Article. Published on 31 ožujka 2023. Downloaded on 8.8.2024. 13:17:39.
This article is licensed under a Creative Commons Attribution-NonCommercial 3.0 Unported Licence.

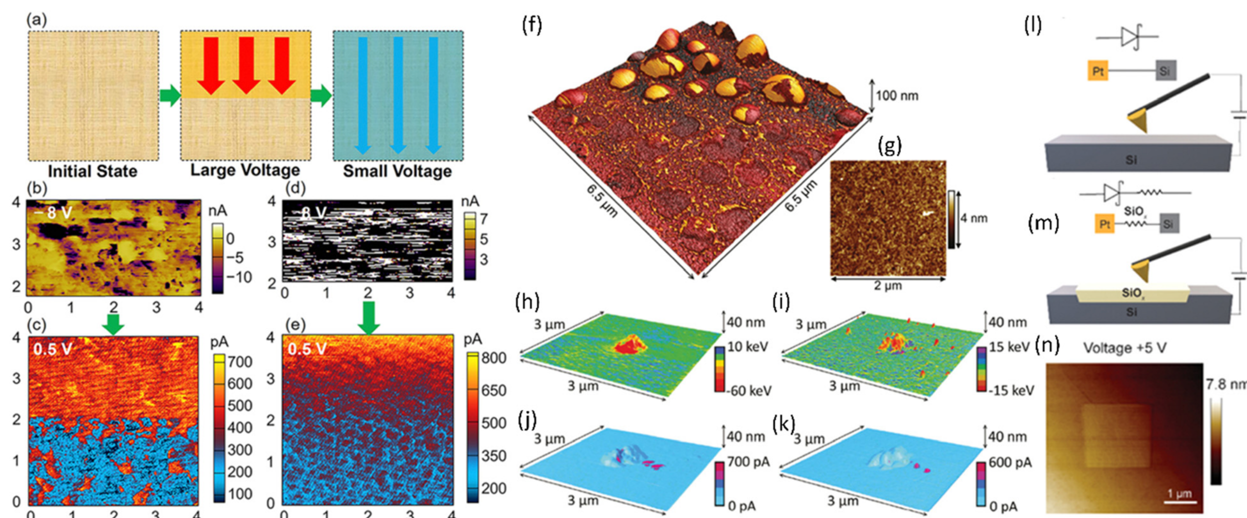

Fig. 3 C-AFM investigation on switching mechanism of $MAPbI_3$-based memristor: (a) diagram of C-AFM measurement procedure, where a large voltage scan is carried out only at the upper part of the square area, and then a low voltage read process is scanned on the entire area. Current mapping images of a $MAPbI_3$/FTO structure with voltage bias of (b) −8 V, (d) +8 V for stressing in the upper area, and (c and e) 0.5 V for corresponding read processes for both biases. Reproduced with permission from ref. 79. Copyright 2018, American Chemical Society. AFM examination on SiO_2-based memristor: (f) AFM topography of the surface of the switching layer SiO_2 after initial bias applied and (g) its pristine counterpart image. Energy dissipation mapping images obtained with (h) a positive-bias initial stressing and (i) a negative one. Associated C-AFM conductivity mapping for (j) positive stressing and (k) negative one. Reproduced with permission from ref. 80. Copyright 2016, published by John Wiley and Sons. This is an open access article distributed under the terms of the Creative Commons CC BY license. *In situ* fabrication and investigation of SiO_x-based memristors directly on Si formed by C-AFM: diagrams for CAFM tip-induced oxidation (l) set up and (m) establishment. (n) Topography of silicon oxide hillocks on Si surface formed by applying 8 min +5 V bias scan. Reproduced with permission from ref. 81. Copyright 2022, American Chemical Society.

size, a +8 V upper scanning and 0.5 V full read process were completed and associated current mapping images are displayed in Fig. 3d and e. The areas were divided into high-bias scanned (high current level) and non-scanned (low current level) parts for both −8 V and +8 V cases. These results indicate that the $MAPbI_3$ functioning layer can be turned on to LRS in both bias directions, which suggests that the resistive switching relies on its own defects of $MAPbI_3$ film due to the fact that if the switching relies on ions from a specific electrode, only one biasing direction (*i.e.*, to the specific electrode) should turn on the device. Also, an interesting phenomenon can be observed by comparing Fig. 3c and e that −8 V SET has a sharp edge between scanned and non-scanned parts and +8 V SET has an indistinct boundary, implying −8 V SET process is more complete than +8 V. This bias dependent behavior is attributed to that the area of the Pt-coated tip is smaller than the bottom electrode, causing an asymmetrical bipolar resistive switching.

Mehonic *et al.* investigated the surface distortion of switching layer after bias applied through AFM in tapping mode.[80] In order to eliminate the need for removing the upper electrode from a specimen after undergoing electrical stress, the SiO_x switching layer was directly subjected to bias *via* a conductive probe, *i.e.*, served as a top electrode. Voltage pulses of either +20 V or −20 V were applied at different locations, thus enabling examination on the effects of both positive and negative biases. As shown in Fig. 3f, bubble-like features with diameters ranging up to hundreds of nanometers were commonly observed in the vicinity of the probe contact point. As comparison, Fig. 3g is the topography image of pristine SiO_x, exhibiting highly flat surface with a 0.2 nm root-mean-square roughness. In some instances, permanent bumps were noticed at the bias point after undergoing electrical stress, these bumps were up to a few hundred nanometers in width and approximately 40 nanometers in height. The energy dissipation mapping can reveal material's mechanical properties such Young's modulus. Thus, the scans of energy dissipation are shown in Fig. 3h for positive bias and Fig. 3i for negative bias. These energy dissipation results suggest that the conductive region is less stiff than the pristine area. Elevated areas were found to dissipate more energy than the original surface under both positive and negative stress. Conversely, some regions demonstrated lower energy dissipation, indicating localized hardening. C-AFM reveals a correlation between surface distortion and areas of elevated conductivity (as demonstrated in Fig. 3j and k). It can be inferred that both positive and negative biases cause an expansion of the oxide layer, which is accompanied by an increase in local conductivity. This implies that Joule heating caused by the flow of current leads to a distortion in the local structure, resulting in surface deformation and regions of varying hardness.[80]

In addition to the surface, electrical and mechanical characterizations for memristor applications, AFM can also form an oxide switching layer directly from a metal species (then becomes a bottom electrode). Peiris *et al.* grew silicon oxide hillocks on Si surfaces by C-AFM tip-induced oxidation to fabricate a silica based memristor.[81] The thickness of oxide film was controlled by the magnitude of the applied bias, duration polarity and the Si doping type, *i.e.*, n-type and p-type.

 © 2023 The Author(s). Published by the Royal Society of Chemistry

Open Access Article. Published on 31 ožujka 2023. Downloaded on 8.8.2024. 13:17:39.
This article is licensed under a Creative Commons Attribution-NonCommercial 3.0 Unported Licence.

Fig. 3l demonstrates the process set up schematically where a positive bias is applied on n-type Si. Fig. 3m pictorially describes an AFM tip-induced silicon oxide hillock is established. For example, with an 8 min +5 V bias scan, the average height for the AFM tip-induced oxide achieved 6.3 ± 0.37 nm, as shown in Fig. 3n. And this kind of AFM tip-induced memristor shows an on/off ratio larger than 10^4.

5. *I–V* DC sweeping

In this section, DC sweep measurements will be reviewed as a typical electrical evaluation of memristors, which can also serve as a great starting point for learning the resistive switching behavior and associated mechanism. Fig. 4a describes a typical *I–V* curve for the most studied bipolar filamentary memristor. The top electrode is connected to the electrical bias and the bottom electrode is grounded. Thus, the ramped voltage stresses are added across the switching layer of the memristor. An as-prepared (or un-biased) memristor is initially in the high resistance state (HRS), or OFF state which can be considered as logic value '0'. With an application of the positive external electrical stress, a formation of conductive filament in the switching layer and the memristor is switched to a low resistance state (LRS), or ON state which can be considered as logic value '1'. This process is referred to as the 'SET' process, and the voltage ignited the transition is called SET voltage (V_{set}). After reaching the LRS, the positive voltage is reduced to 0, and increase negatively to enable another transition. At certain negative bias, a RESET voltage (V_{reset}), the conductive filament is ruptured, and the LRS of the memristor is switched back to initial HRS, *i.e.*, a RESET process is established. During the forward and backward sweeps, the current values are checked at the same voltage, typically ∼0.1 V, which turns out that there is a gap between these two current levels. This current checking is called "read", and the resistances (R_{HRS} and R_{LRS}) at two states can be simply calculated with the read voltage (∼0.1 V) and current values. It is worth noting that a limited current (compliance current) was usually employed during the DC sweeping for collecting hysteretic *I–V* curves. And the compliance current can prevent an irreversible hard break on the memristor.[82–84] Fig. 4b presents one cycle of *I–V* sweeping characteristics in linear scale of an $Ag/HfO_2/Pt$ memristor with associated schematic elucidation of its switching mechanism.[85] It clearly introduces the relations between the electrochemical processes and each switching state in the electrical characteristics. With a positive bias, the top electrode, chemically active Ag, is partially oxidized as Ag+ ions. And then, these Ag+ ions migrate towards the bottom noble Pt, and are reduced to Ag atoms there. The accumulated Ag atoms form conductive filaments across the dielectric layer and a SET process is completed. Thus, in the LRS, the memristor exhibits an ohmic transport mechanism. When a negative bias is applied to the top Ag electrode, the oxidation of Ag filaments into Ag+ ions and reduction at the Ag electrode reversibly occurred, which led to the rupture of the filament conduction path and switching these devices to an OFF state (RESET process). DC sweeping *I–V* evaluation is often plotted as the logarithm of currents' absolute values *vs.* linear voltage values which is called semi-log or butterfly graph. In this way, the R_{LRS}/R_{HRS} ratio is visualized much more clearly. Fig. 4c is a semi-log presentation of the measurement for a SiO_2/Ta_2O_5 based memristor.[86] 1000 cycles of DC sweeping data are all plotted in the butterfly graph. The plot commonly shows the variation of each cycle, it is reasonable to highlight typical cycles, such as the first and last cycle, as Fig. 4c does, or the average/fit of all cycles. Fig. 4d

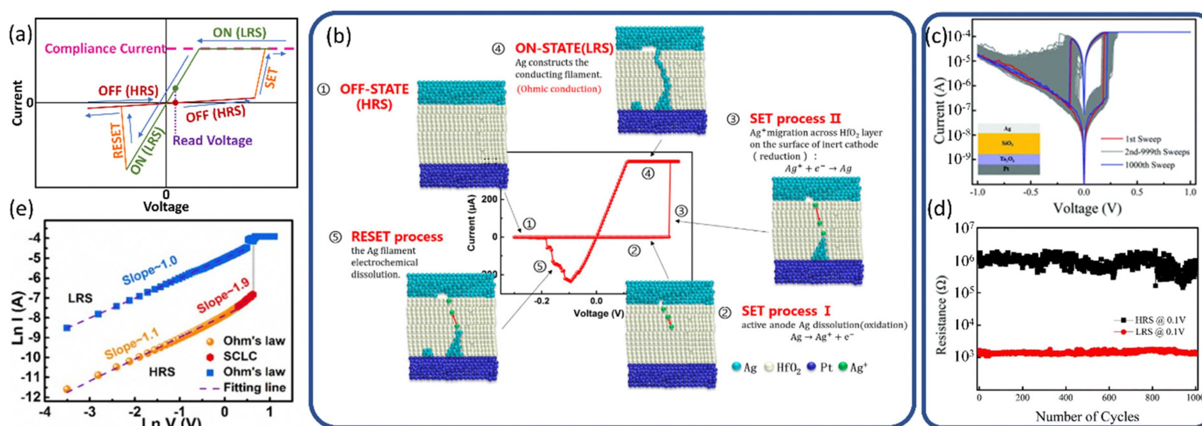

Fig. 4 Elaboration of DC sweeping *I–V* characterization. (a) A detailed explanation of a typical *I–V* curve in linear–linear scale from DC sweeping, indicating bipolar resistive switching. (b) Actual DC sweeping *I–V* characteristics and corresponding switching mechanism of an $Ag/HfO_2/Pt$ memristor. Reproduced with permission from ref. 85. Copyright 2018, published by MDPI. This article is an open access article distributed under the terms and conditions of the Creative Commons Attribution (CC BY) license, a SiO_2/Ta_2O_5 based memristor, showcasing (c) 1000 cycles of DC sweeping data plotted in semi-log scale (linear scale *x*-axis and log scale *y*-axis). The curves of all cycles are displayed and the first and last cycles are highlighted. (d) Associated endurance characteristics obtained from resistance values read at 0.1 V at HRS and LRS. Reproduced with permission from ref. 86. Copyright 2020, The Royal Society of Chemistry, and (e) Double-log scale analysis for an Ag/ZnO/ITO memristor, where the slopes of HRS and LRS determine the α value in the $I \propto V_\alpha$, indicating the conduction mechanism. Reproduced with permission from ref. 99. Copyright 2021, Elsevier.

Open Access Article. Published on 31 ožujka 2023. Downloaded on 8.8.2024. 13:17:39.
This article is licensed under a Creative Commons Attribution-NonCommercial 3.0 Unported Licence.

summarizes the distribution of resistance values of SiO_2/Ta_2O_5 based memristor at HRS and LRS along with the cycle number, *i.e.*, endurance behavior, which is extracted from *I*–*V* measurements at 0.1 V. The endurance characterization visualizes the on/off ratio, switching variation, and cycling number during the repeated DC sweeping in a more quantitative way. When the semi-log and endurance characteristics are reported, the data in very cycle should be included, especially, only 100 cycles are presented for DC sweeping commonly. It should be noted that measured R_{HRS} and R_{LRS} in each cycle should be all reported. If one uses only one data point to present 10 cycles of data, it is possible that some failure cycles occur within 10 cycles, thus, the endurance is overestimated. This issue is also noticed in another article, and the authors argued that measuring and reporting endurance for every cycle is especially important for advanced materials (*e.g.*, 2D materials, perovskites, MXenes)[87–92] based memristors and nanostructured (*e.g.*, nanowires and nanotubes)[93–96] memristors as their switching mechanisms and their reliability have not been demonstrated by other groups and not been established.[97] Therefore, the performance of these devices requires further objective evaluations as the performance since related mechanisms are controversial and not widely accepted. The DC sweeping data can be interpreted in double logarithm scale to analyze the conduction mechanisms.[98] For example, in the Fig. 4e, the DC sweeping current–voltage curves from an Ag/ZnO/ITO memristor was plotted in double logarithmic coordinates during the SET process.[99] During initial HRS within low positive bias region, the current flowing shows a linear relationship ($I \propto V$, *i.e.*, the slope is around 1) indicating an ohmic conduction mechanism, corresponding to thermally generated carriers. Along with an increasing bias, the slope of the current–voltage curve increases to 1.9, *i.e.*, $I \propto V^2$, which implies that the current flowing follows a space charge limit current (SCLC) conduction mechanism before the HRS/LRS transition.[99,100] When Ag filaments were formed, the memristor transitioned to LRS and the slope became 1 again, followed Ohm's law. Although the DC sweeping is a basic characterization for memristor, this measurement can reveal key information such as endurance, variation and conduction mechanism with different interpretations.

6. Pulse

As reviewed in the previous section, a variety of information can be retrieved by utilizing DC sweeping characterization. However, the slow DC ramping may be not suitable for most of the practical electronics applications. Lanza *et al.* claimed that if the memristor device fails to switch within 1 microsecond, it becomes not useful for the majority of resistance switching technologies.[97] In addition, many reports claim that 10^6 or higher endurance performance, thus, through time-consuming DC sweeping is not a realistic approach for measuring such a high number of switching cycles.[101–107]

Pulse measurements are instrumental to address these issues Fig. 5a is a typical endurance characteristics plot employing the pulse technique, obtained from cellulose nanocrystal (CNC)-based memristor.[108] The *x*-axis represents the pulse number and *y*-axis is labeled for resistance, or other equivalent information such as current, or conductance. A typical scheme of a pulse train for endurance characterization is shown in Fig. 5b, which includes the cycle as follows: a READ pulse, a SET pulse, a READ pulse, a RESET pulse, and a READ pulse.[97] And sufficient number of data points is also crucial since insufficient data points (*i.e.*, with low resolution) may not be able to identify the SET/RESET behaviors. In Fig. 5b, the SET/RESET processes are exampled with the adequately large number of points, showing detailed switching behaviors. However, a large volume of data often limits obtaining pulse measurements beyond a certain number of data points. Therefore, optimizing the size of data while being able to demonstrate the performance profile is required. Despite the practical usefulness of pulse measurements as a memristor characterization, we notice two major issues. First, READ pulse is missing in the pulse scheme. Second, the result does not report all the resistance values for the whole cycling test. These data exhibitions are not recommended.

Another major application of pulse measurements for memristors is to characterize the synaptic weight updating, especially for neuromorphic computing applications.[109–116] Typical plots of synaptic weight updating process are displayed in Fig. 5c.[117] In principle, this characteristic demonstrates a series of SET (long-term potentiation (LTP)) and RESET (long-term depression (LTD)) processes of the memristor with repeated pulses. The representative scheme of the pulse train for a cycle of LTP and LTD is shown in Fig. 5d. If we temporarily ignore the READ pulse for an easier comparison, the pulse train scheme for endurance is a (1 SET + 1 RESET) $\times$ *N* pattern, however, for the LTP/LTD characterization, it is a (1 SET $\times$ *n* + 1 RESET $\times$ *n*) $\times$ *N* pattern where *n* is the continuous count number for one polarization and *N* is the cycling number. For instance, in Fig. 5d, one LTP/LTD cycle contains 1000 times of −15 V pulses with 5 ms pulse width, followed by 1000 times of 2 ms + 10 V pulses, thus, n = 1000. And in Fig. 5c, the plot shows three cycles of LTP/LTD, *i.e.*, N = 3. Fig. 5e suggests that the characteristics can be tuned/optimized by the modulate the pulse's width and amplitudes.

We recommend that researchers should provide a detailed description, including diagrams, of the pulse train scheme, testing setup circuit, data recording resolution, and all resistance values obtained in endurance testing. This information helps other researchers understand the methodology and replication of the study and provides transparency and accountability in the research process.

7. Image processing

The characterization techniques reviewed in the preceding sections are focused on the single-device level. An increasing

 © 2023 The Author(s). Published by the Royal Society of Chemistry

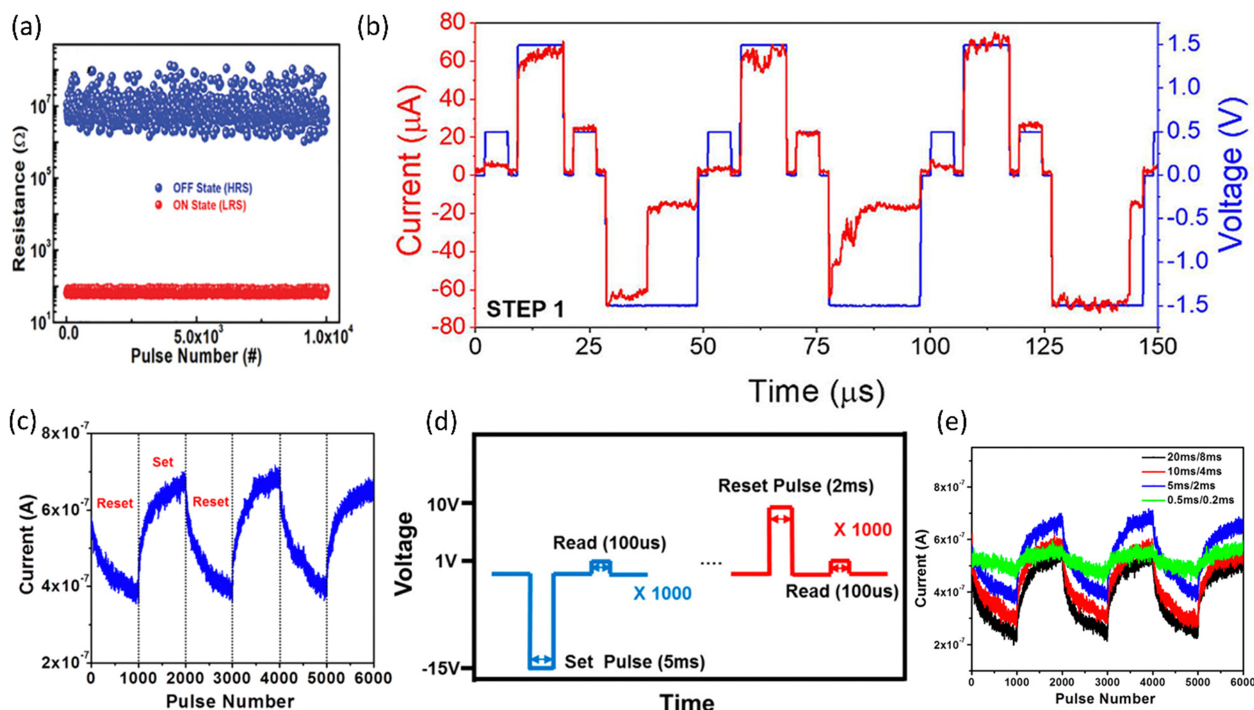

Fig. 5 Demonstration of pulse measurements for endurance and linearity characterization. A typical endurance characteristic of a memristor with a pulse, enabling a large number of cycling: (a) a pulse-measured endurance characteristics of a cellulose nanocrystal (CNC)-based memristor with 104 pulse cycles. Reproduced with permission from ref. 108. Copyright 2021, John Wiley and Sons, (b) a segment of pulse endurance characteristics. A blue pattern represents the applied pulse scheme and a red pattern provides the recorded current values. The smaller amplitudes of pulses are READ pulses. And the larger ones are SET/RESET pulses. Reproduced with permission from ref. 97. Copyright 2021, published by American Chemical Society. This article is an open access article distributed under the terms and conditions of the Creative Commons Attribution (CC BY-NC-ND 4.0) license; and linearity testing on MoS_2-based memristor: (c) a pulse characteristic of the LTP/LTD process of a MoS_2-based memristor. (d) Pulse train profiles for the LTP/LTD testing. 1000 continuous identical negative SET pulses and READ pulses followed by 1000 continuous identical positive RESET pulses and READ pulses. (e) LTP/LTD characteristics measured from the same MoS_2-based memristor, under various SET/RESET pulse width combinations. SET and RESET pulse amplitudes are −15 and +10 V, respectively for all measurements. Reproduced with permission from ref. 117. Copyright 2018, American Chemical Society.

Open Access Article. Published on 31 ožujka 2023. Downloaded on 8.8.2024. 13:17:39.
This article is licensed under a Creative Commons Attribution-NonCommercial 3.0 Unported Licence.

number of studies have shown brain-inspired computing such as deep neural networks (DNNs) were realized by utilizing memristive crossbars.[118–125] Therefore, image processing is considered a characterization technique for demonstrating the advanced capabilities of memristors. Xia and Yang summarized fundamental knowledge of neuromorphic computing, and key concepts are reintroduced here concisely.[126] Fig. 6a is a schematic of a simple neural network. The input layer neurons receive signals and transmit them to the neurons in the hidden layers that have a nonlinear activation function to process the weighted sum and send them to the output layer. The synaptic weights W_{ij} can be tuned during training to minimize the error between the output and known targets by gradient descent algorithm. This kind of brain-inspired computing function can be realized with a memristive crossbar by performing vector–matrix multiplication, as shown in Fig. 6b. In principle, according to Ohm's law ($I = VG$), an input voltage vector is applied to each junction with varying conductance (G) (*i.e.*, a conductance matrix), resulting in a current. While the conductance is always positive, synaptic weights can be negative in a memristive neural network, thus, the weights are commonly depicted by the conductance difference between two devices called a differential pair. Prezioso *et al.* demonstrated a fully operational neural network by utilizing a memristive crossbar with a Al_2O_3/TiO_{2-x}-based memristor at each cross point to classify the 3 × 3 binary (black or white) patterns in Fig. 6c.[127] This single-layer perceptron contains ten inputs and three outputs, which were fully connected with 30 synaptic weights (*i.e.*, 10 × 3 = 30) as shown in Fig. 6d. As illustrated in the scheme, the perceptron's outputs f_i (with i = 1, 2, 3) are computed using nonlinear activation function, $f_i = \tanh(\beta I_i)$, and where the vector-by-matrix product components, $I_i = \sum_{j=1}^{10} W_{ij} V_j$. The input signals are denoted by V_j with j = 1,...,9. V_{10} is a constant bias for accelerating the convergence process and the function's nonlinearity is controlled by β, finally, the adjustable (trainable) synaptic weights are labeled as W_{ij}. This type of network is capable of classifying 3 × 3-pixel black and white images into three classes, with nine inputs corresponding to the pixel values. Three stylized letters '*z*', '*v*' and '*n*' were tested on this network with 30 patterns (three sets) displayed in Fig. 6c. For example, there are a set of 10 versions of letter *z* and the first one in this set is the correct one. The rest 9 versions are the noisy (incorrect) ones, formed by flipping one of the pixels of

Open Access Article. Published on 31 ožujka 2023. Downloaded on 8.8.2024. 13:17:39.
This article is licensed under a Creative Commons Attribution-NonCommercial 3.0 Unported Licence.

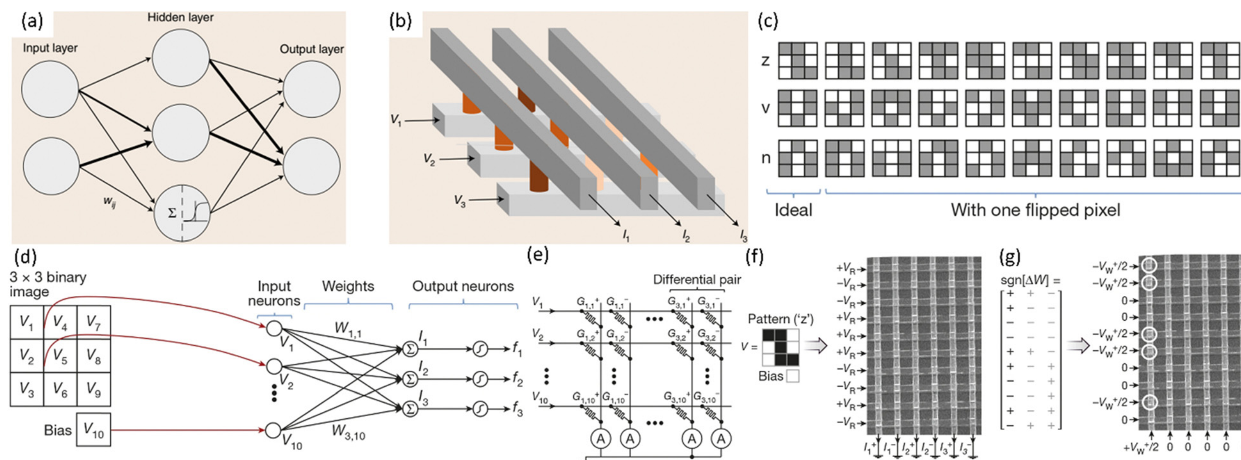

Fig. 6 Image processing fundamentals with memristor-based neuromorphic computing. (a) A simple neural network diagram. (b) A demonstration of the neural network on a memristive crossbar. Note, different shades of orange indicate different conductance at each junction. Reproduced with permission from ref. 126. Copyright 2019, Springer Nature, and image classification with metal-oxide memristors: (c) 3 × 3 binary image sets. (d) The schematic of single-layer perceptron for image classification. (e) Circuit demonstration of a 10 × 6 fragment of a memristive crossbar for this single-layer perceptron. (f) An illustration of the classification process for a specific input pattern (in this case, a stylized letter 'z'), using input signals of +VR or −VR on the Al_2O_3/TiO_{2-x} memristive crossbar, depending on the color of the pixel. (g) An illustration of the process of adjusting the weights in a specific column (in this case, the first positive column) based on a specific error matrix by using set/reset pulse $V_{W\pm}$ = ±1.3 V. Reproduced with permission from ref. 127. Copyright 2015, Springer Nature.

the correct image. These sets were used for both training and testing due to the small set size. The bias input V_{10} was set to −0.1 V. Each input signal, voltage V_j was equal to either +0.1 V ($+V_R$) or −0.1 V ($-V_R$), corresponding to the black or white pixel respectively. Every two memristors are considered as a differential pair, a total of 60 memristors in the crossbar (30 × 2 = 60) were drawn in Fig. 6e. Fig. 6f elaborates an operation for pattern *z*. The input voltages can be determined by previously described rules and were applied to cross bar, and the resulting currents for each column (each top electrode bar) were evaluated then convert to perceptron's outputs with an activation function. These outputs were compared with the preset label values for letter *z*, *n*, *v* to get the differences which are known as the loss functions. Based on the loss function, back-calculate the adjustments of each weight using the gradient descent algorithm. This process is known as the back-propagation process. Fig. 6g presents the next step: the adjustments were physically established by using set pulse and reset pulse to tune the conductance of the synapses. When the output signal for the correct class of the applied pattern was higher than the signals for all other classes, the perfect classification was reached, on average, after 23 training epochs. It should be noted that the training of the network was performed *in situ*, without using an external computer model. Although this is a simple neural network only with one layer, it is a classical case study for examining if one possesses enough prerequisite knowledge about the algorithm to conduct advanced image processing characterizations. More importantly, it can be inferred that good reliability at single device level is required because realizing neural network on a memristive crossbar basically involves manipulations of numerous memristors with multiple conductance levels. Hence, the fundamental study on memristor at single device level remains of paramount importance. If researchers do not have access to crossbar fabrication, or prefer to work on optimizing performance at single device level, one can simulate the image processing performance like recognizing handwriting numbers for a single device level of memristor study by using an in-house software or simulator such as CrossSim.[39,128–133]

8. Cyclic voltammetry (CV) and electrochemical impedance spectroscopy (EIS)

Cyclic voltammetry (CV) and Electrochemical Impedance Spectroscopy (EIS) are widely used to characterize electrochemical behaviors in various fields such as corrosion, electrocatalysis and battery.[134–139] CV and EIS have also been employed to characterize the electrochemical behavior of memristors and hence enhance an understanding of the memristor behavior.[140–144]

In memristor investigations, CV measurements can give insight into the redox processes happening before the switch events.[145] Lübben *et al.* examined the electrochemical redox characteristics of various metals as active electrode materials within a M/SiO_2/Pt system (M represents metal) spanning from noble to transition metals.[145] Fig. 7a summarizes the CVs of metal electrodes, demonstrating no significant passivation effects, *i.e.*, no interfacial oxide was formed, indicating a reversible process. The general pattern is that the lower the nobility of a metal, the greater the negative potential required for reduction processes, with V, Ni, Fe, Cu, Ag, and Au ordered from most negative to most positive cell potential, with Au

 © 2023 The Author(s). Published by the Royal Society of Chemistry

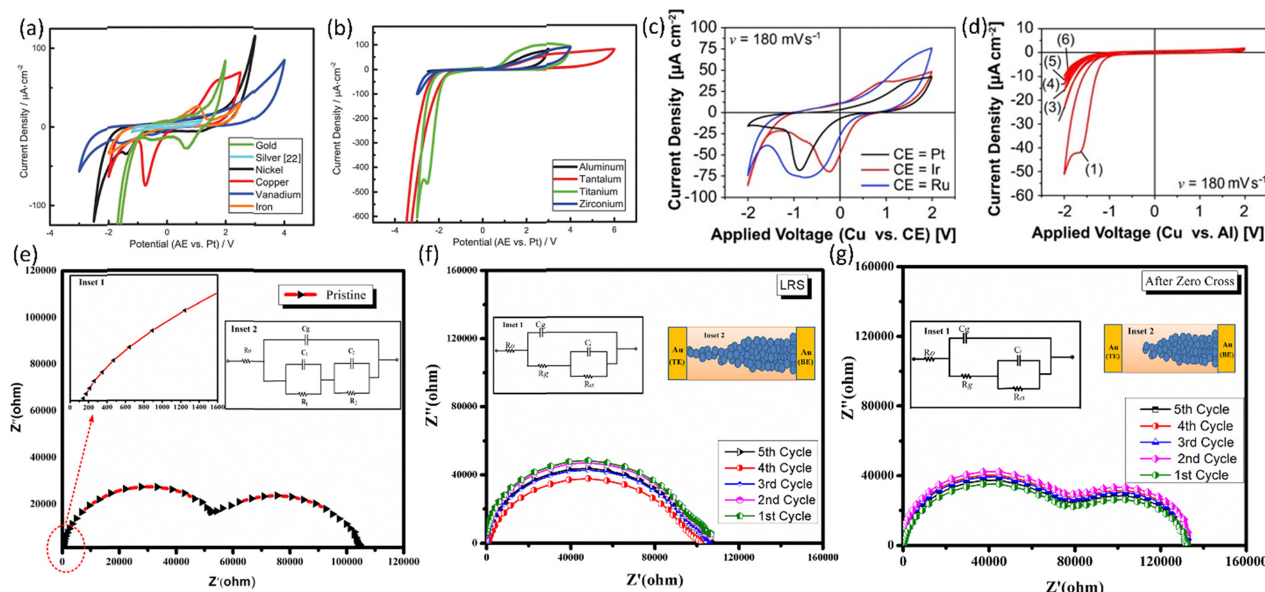

Fig. 7 Interpretation of CV and EIS characterizations with exemplary works. Comparison and categorization of the CV of the tested active electrode materials in SiO_2-based memristors which can be classified based on their redox behavior: (a) reversible process, meaning that no passive film is formed, and the species can return to its original state. (b) Irreversible oxidation, where the formed product cannot be restored to its initial chemical state. Reproduced with permission from ref. 145. Copyright 2019, John Wiley and Sons, Influence of the CE material on the redox reactions preceding resistive switching: (c) CV plots of Cu/SiO_2/CE memristors with various inert CE materials (Pt, Ir, and Ru). (d) Al, a passive metal that may form an interfacial oxide, as CE. Reproduced with permission from ref. 146. Copyright 2014, John Wiley and Sons, and EIS measurements on different states of Au/TiO_{2-x}/TiO_2/Au memristor: (e) EIS characteristics of the pristine device. Inset 1 displays a high-frequency spectrum. Inset 2 is the equivalent circuit. (f) After the SET process, A single contour was observed, revealing the device retained at LRS. The associated equivalent circuit is displayed in inset 1. Inset 2 is a schematic for LRS. (g) After the reverse voltage passed zero, two semicircles appeared, indicating the initiation of rupturing of filaments. The insets again demonstrate the equivalent circuit and schematic for the testing state. Reproduced with permission from ref. 150. Copyright 2018, Elsevier.

having the highest positive potential. The reaction rate varies among the active metals, with Cu, V, Au, and Ni having higher reaction rates, and Fe and Ag being less electrochemically active. Determining a clear order for oxidation reactions is difficult as most metals don't exhibit a prominent oxidation peak. Fig. 7b compares the cyclic voltammograms of active electrode metals with high oxygen affinity. The first cycles are analyzed as they determine the formation of a passive film that impacts the shape and intensity of the CV curves. The potentials and currents of the peaks give insight into the redox reactions' thermodynamic driving force and reaction rate. For instance, aluminum rapidly begins oxidation, but its dense barrier-type layer significantly reduces current and further oxidation. A 2–3 nm interfacial Al_2O_3 film is enough to passivate the device. In contrast, tantalum shows slower reaction rate, but can be oxidized over a wider voltage range to form oxide films up to several tens of nanometers, still permitting ionic motion. Titanium and Zirconium exhibit oxidation behavior between aluminum and tantalum, with Zr showing lower current densities and faster passivation compared to titanium. It's crucial to note that the crystallographic and defect-chemical structure of the interfaces formed also influences the device properties, not just the oxidation potentials. The choice of the counter electrode is equally important as the active electrode due to the electrochemical nature of filament formation.[146,147] The starting point of filament formation is the counter electrode (typically BE), which is negatively biased during the SET process. The counter electrode's ability to catalyze reduction reactions is critical to the process.[147] Cyclic voltammograms for various counter electrode materials of Cu/SiO_2/CE (CE represent counter electrode) memristors are reported by Valov *et al.*, of which the plots for noble metals are shown in Fig. 7c and Al in Fig. 7d.[146,147] As shown, noble metal electrodes exhibit varying catalytic activity, with Ir being the most active followed by Ru, then Pt. From an electrochemical standpoint, devices using Ir or Ru electrodes should perform better, particularly in terms of switching time since their CV curves contained higher current density (j) peak than the Pt.[147] Electrodes with a high affinity for oxygen, such as Al, are prone to passivation and inhibit further reactions. The results indicate that the counter electrode reaction rate is lower compared to that of the active electrode, which determines the reaction rate of the overall system. Increasing the counter electrode reaction rate leads to a higher reaction rate in the active electrode and, therefore, a shorter switching time. From the analysis above, we can see that CV measurements can be effective to provide foundational reference information for the selection of electrodes.

The purpose of EIS is to analyze electrochemical systems and gain insight into the underlying electrochemical processes by measuring impedance changes at different sinusoidal frequencies.[148] Accurate modeling is crucial to interpret the

Open Access Article. Published on 31 ožujka 2023. Downloaded on 8.8.2024. 13:17:39.
This article is licensed under a Creative Commons Attribution-NonCommercial 3.0 Unported Licence.

Open Access Article. Published on 31 ožujka 2023. Downloaded on 8.8.2024. 13:17:39.
This article is licensed under a Creative Commons Attribution-NonCommercial 3.0 Unported Licence.

data, which is often accomplished through the use of equivalent circuit models.[148] This non-invasive evaluation technique transforms EIS data into meaningful parameters such as capacitance (C), resistance (R), and constant phase element (CPE) that describe the electrochemical process.[148] Nyquist plots, generated through EIS, effectively display the relationship between impedance and frequency.[149] By using EIS to analyze memristor devices, which change their resistance in response to an applied electric field in a range of frequencies, we can gain insight into the different resistive regimes related to their switching behavior (SET/RESET). This nondestructive approach allows us to provide additional or supplementary evidence of the results obtained using TEM investigations which often require exquisite manipulations of the samples and specific accessories for memristive behaviors imaging.[150] The impedance response of pristine Au/TiO_{2-x}/TiO_2/Au memristor cells was measured by Dash *et al.* at equilibrium (zero applied bias) to examine Z'' *vs.* Z, where Z'' is the imaginary part and Z' is the real part of the impedance, at frequencies ranging from 1 MHz to 10 mHz.[150] The results in Fig. 7e show two distinct resistive regimes in the Nyquist plot, confirmed by two semicircular frequency dispersion contours, likely attributed to the bilayer of TiO_{2-x} and TiO_2. The frequency dispersion was well within the bulk impedance response of resistive/capacitive. The resistance values of 57 kΩ and 65 kΩ for contour 1 and 2 respectively, indicate the relative resistances of non-stoichiometric TiO_{2-x} and stoichiometric TiO_2. To gain a deeper understanding of the impedance response at different switching states, impedance measurements were conducted as an *ex situ* analysis by interrupting the potential sweep at points where resistive changes occur. The resulting data showed a single impedance contour, which suggests the presence of a single charge transfer resistance (R_{ct}) and interfacial capacitance connected in parallel, indicating that the formation of a filamentary galvanic contact with the TE had occurred. As depicted in inset 1 of Fig. 7f, this is supported by the equivalent circuit model. The researchers then applied a reverse voltage towards zero, and upon passing zero, they performed another EIS measurement. The spectrum returned to its original pristine-like state, with two clearly distinguishable impedance contours as shown in Fig. 7g.

Part II. Reliability issues in memristors

9. Endurance

Endurance is a key metric in evaluating a memristor's reliability, defined as the maximum number of cycles before failure occurs.[151] However, most of the memristors suffer endurance degradation and/or failure after a number of switching cycles. The endurance is usually visualized by resistance/conductance *versus* cycle number graph. Chen *et al.* observed and categorized endurance failure symptoms into three types for their transition metal oxide (TMO)-based memristors with TiN and Pt electrodes: in Type I, R_{HRS} decreasing and R_{LRS} increasing occur simultaneously; in Type II, R_{LRS} remains stable and R_{HRS} decreases and R_{HRS} suddenly drops to R_{LRS}'s level; and in Type III, R_{LRS} keeps stable and R_{HRS} gradually decreases to R_{LRS}'s level.[152] Fadeeva and Rudenko also point out another two types of endurance failure/degradation symptoms which are basically opposite behaviors of Type II and Type III, meaning that R_{HRS} is stable but R_{LRS} increases gradually (Type V) or more abruptly (Type IV).[153] These five types of failure and degradation behaviors are illustrated in Fig. 8(a–e) with trend lines. Fig. 8(f–j) present the practical examples of the associated categories.[154] Physical mechanisms were suggested to understand these failure/degradation behaviors and these mechanisms are schematically explained in Fig. 8(k–n). Due to the nature of the TMO switching layer and noble electrodes, oxygen-related mechanisms govern the failures of Type I, II, and III.[152] Type I is caused by a metal oxide barrier formed by Joule heating and oxygen ions creation during the forming processing, which blocks the transportation of electrons and oxygen ions.[152] Type II can be explained as excess oxygen vacancies induced by an electrical field, which thickens the conductive filaments.[152] Type III is attributable to the overabundant depletion of oxygen ions, caused by RESET processes, thus, reducing the likelihood of recombination between oxygen ions and oxygen vacancies and hence rupture of the conduction filament.[152] The Type IV degradation of LRS is accounted by Zhao *et al.* for the presence of unrepairable and large gaps caused by the exhaustion of oxygen vacancies (Fig. 8n).[151] They also describe an endurance evolution with the different voltage programming conditions, causing different failure/degradation types (Fig. 8o). Type II and III are also classified as stuck-at-LRS while Type IV and V as stuck-at-HRS, and Type I as stuck-at-MRS (MRS represents medium resistance state). Among them, stuck-at-LRS is the most common failure type, relating the unruptured conduction filament.

The strategies for improving cycling endurance are desirable and enhanced endurance has been accomplished.[155–162] For example, Kumar *et al.* demonstrated an improvement in endurance of about three orders of magnitude by modifying the device structure.[163] The initial memristor structure consisted of Pt/TiN/HfO/Pt. With voltage pulse, the device ultimately malfunctioned by becoming permanently stuck in the ON state (stuck-at-LRS) after approximately 2 million cycles and was unable to be restored even when higher levels of DC bias were applied (Fig. 8p). Fig. 8q is the image of the failed device obtained through scanning transmission X-ray microscopy, where substantial fluctuations in intensity were observed, indicating widespread morphological disorder. Further X-ray and AFM analyses identified electrode damage as well as the separation and movement of oxygen. The failure in switching was likely due to one or more clusters that were highly lacking in oxygen becoming highly conductive and causing the electrodes to short permanently. To create a more consistent reservoir for excess oxygen and to prevent the formation of clusters, they increased the thickness of the TiN electrode layer. In addition, to accommodate high voltage or power spikes with a minimal temperature increase during memristor cycles, the thickness of

 © 2023 The Author(s). Published by the Royal Society of Chemistry

Open Access Article. Published on 31 ožujka 2023. Downloaded on 8.8.2024. 13:17:39.
This article is licensed under a Creative Commons Attribution-NonCommercial 3.0 Unported Licence.

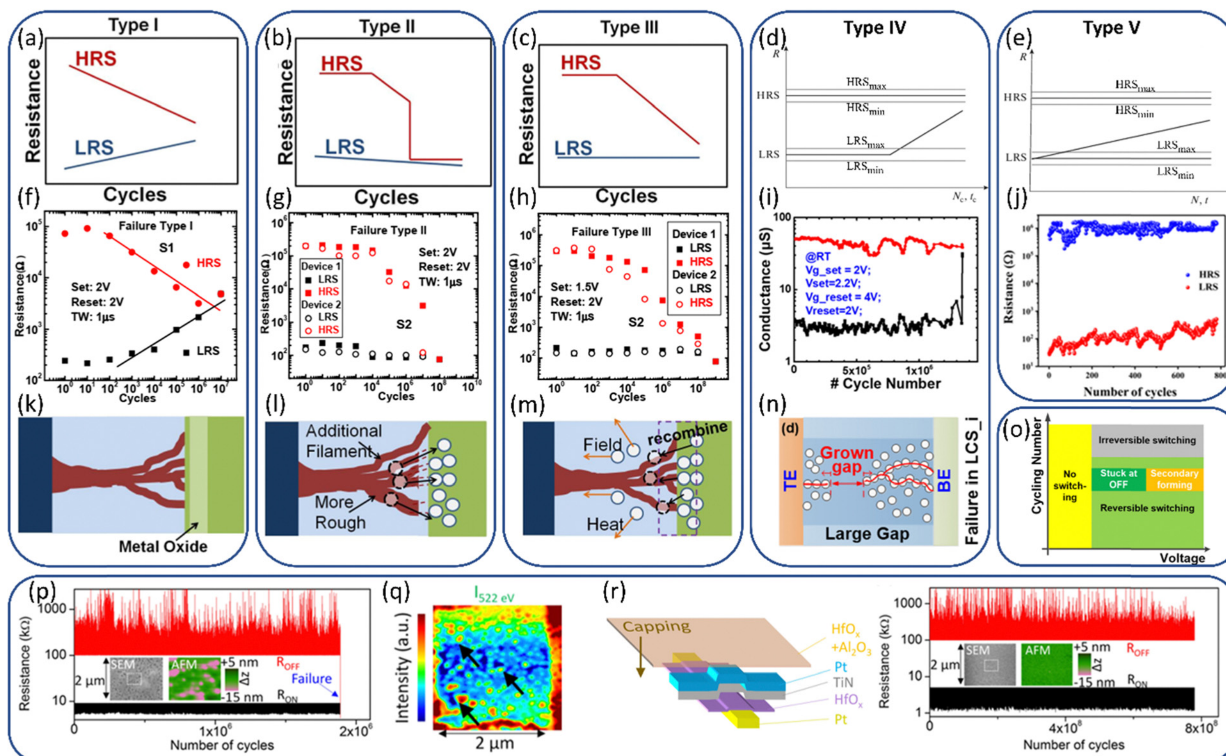

Fig. 8 The failure modes associated with actual memristor failures, mechanisms and improvements in cycling endurance. Type I: (a) failure mode demonstration. Both RHRS and RLRS degrade and meet in the middle. (f) Measured data from TiN/HfO_x/Pt memristor, with +2 V SET and −2 V RESET pulses, pulse time width (TW) is 1 μs. Note, RESET 2 V in the figure only represents its magnitude. This is also true for (g and h). (k) Illustration of failure mechanism. Type II: (b) trend lines for a sudden RRHS degradation mode. (g) Measured data from TiN/HfO_x/TiO_x/HfO_x/TiO_x/Pt memristor. The testing condition is the same as (f). (l) Schematic of failure mechanism. Solid line circles represent oxygen ions and dashed lines are oxygen vacancies. Type III: (c) graph of the gradual RRHS degradation mode. (h) Measured data from TiN/HfO_x/Pt memristor, with +1.5 V SET and −2 V RESET pulses, pulse TW is 1 μs. (m) Corresponding mechanism explanation. The squared area with a dashed line is the interface between the switching layer and the electrode. Reproduced with permission from ref. 152. Copyright 2011, IEEE. Type IV: (d) failure mode illustration of steep RLRS degradation. (i) Measured data from HfO_2/Al_2O_3 multilayer memristor with a transistor (1T1R). (n) Associated failure mechanism elaboration. White circles represent oxygen vacancies. And red lines symbolize conduction paths. (d) Reproduced with permission from ref. 153. Copyright 2021, published by Springer Nature. This is an open access article distributed under the terms of the Creative Commons CC BY license; (i and n) Reproduced with permission from ref. 151. Copyright 2019, published by IEEE. This is an open access article distributed under the terms of the Creative Commons CC BY license; Type V: (e) presentation of failure mechanisms of gradual HLRS degradation. (j) Measured data from K-birnessite MnO_2-based memristor. (e) Reproduced with permission from ref. 153. Copyright 2021, published by Springer Nature. This is an open access article distributed under the terms of the Creative Commons CC BY license. (j) Reproduced with permission from ref. 154. Copyright 2020, American Chemical Society; (o) diagram of endurance *versus* operation voltage conditions describing the device states in (i). Reproduced with permission from ref. 151. Copyright 2019, published by IEEE. This is an open access article distributed under the terms of the Creative Commons CC BY license; and an example of endurance improvement: (p) Endurance characteristics of the reference device, a HfO_x-based memristor. After about 2×10^6 times cycling, the device encounters a stuck-at-LRS failure. The insets are associated SEM and AFM images obtained from failed devices, indicating severe damage to the top electrode. (q) Is the corresponding image by using scanning transmission X-ray microscopy, from which intensive morphology disorder was identified. (r) On the left, it is a schematic of redesigned HfO_x-based memristor, and with the new structure, the cycling number increased up to $\sim 10^9$, shown on the right. Reproduced with permission from ref. 164. Copyright 2017, AIP Publishing.

the Pt electrodes was increased as well. Then, to make the top electrode more stable in terms of delamination or deformation, a capping layer of HfO_x + Al_2O_3 was applied to cover the top electrode and the entire device. With the new device structure (Fig. 8r), the memristor exhibited repeated switching up to 10^9 cycles (Fig. 8r). Fujii *et al.* evaluated and compared cycling endurance for the SiO_2 based memristors with various dimensions of the switching layer (*i.e.*, SiO_2).[164] They found that cycling endurance was improved with scaling down the memristor's dimension. The device with a 30 nm size showed a cycling endurance of 10^4 cycles, while the one with 100 nm size experienced a much earlier failure after about 10^2 cycles. All devices ultimately experienced a RESET failure, *i.e.*, stuck-at-LRS, suggesting the strong conductive filament was eventually formed and could not be ruptured, leading to a failure. Another failure was reported for SiO_2-based memristors with Cu ions excessively doped into the switching layer, of which the stuck-at-LRS failure was also mitigated by scaling down the device. A spatial limitation in a smaller device may suppress the excessive injection and accumulation of Cu ions.

10. Variation

Memristors typically exhibit undesirable variations in resistance values and SET and RESET voltages from one device to

Open Access Article. Published on 31 ožujka 2023. Downloaded on 8.8.2024. 13:17:39.
This article is licensed under a Creative Commons Attribution-NonCommercial 3.0 Unported Licence.

device (also called D2D or spatial variation) and from one cycle to cycle (also called C2C or temporal variation).[165,166] From the perspective of physical mechanism, the cycle-to-cycle variation originates from the stochastic formation and rupture of conductive filaments.[43] The device-to-device variation stems from the limitations of fabrication techniques, which produce non-ideal film morphology and homogeneity, resulting in the different electrical characteristics between memristors.[167] It has been shown that by initializing plasma treatment, varying metallization, or inserting another layer, the temporal variation in *I–V* performance can be reduced.[168–171]

Zhang *et al.* reported an improvement on the variation of IGZO-based memristor by nitrogen plasma treatment.[169] For the reference Pt/IGZO/TiN memristor (untreated control sample), the *I–V* curves in Fig. 9a indicate that the switching parameters are not consistent, showing significant SET/RESET voltage variations over 100 cycles of DC sweeping. As a strategy to mitigate the variation, plasma treatment, generated from a mixed gas of N_2 : Ar (ratio of 50 : 12), was applied to modify the switching layer of IGZO. Before the plasma treatment, the sample was kept in the sputter chamber to limit exposure to air and undesirable any surface contaminations. As a result, an IGZO:N film was obtained after a plasma treatment time of 30 seconds. Subsequently, an additional 18 nm IGZO layer was deposited through sputtering. Fig. 9b shows the *I–V* characteristics for the Pt/IGZO/IGZO:N/TiN memristor, from which less variation on switching behaviors can be observed in Fig. 9b. And the distribution of the set voltages is statistically analyzed in Fig. 9c. It was observed that the IGZO:N device exhibits a narrower distribution of V_{set} in the range of 0.65 V to 0.75 V. In contrast, the distribution of V_{set} is much larger, 0.3–1.3 V in the untreated IGZO memristor. A model was established to clarify the contribution of the IGZO:N inserting layer on the enhanced variation. The model in Fig. 9d depicts the formation of oxygen vacancies that connect the Pt and TiN electrodes in the forming process. During operation, the connection and breaking of this oxygen-vacancy filament cause oxidation and reduction reactions (*i.e.*, redox process) near the TiN electrode. In the Pt/IGZO/TiN device, the oxygen vacancies are recovered randomly, leading to widely distributed Vset and poor uniformity, particularly in HRS, as shown in Fig. 9d (left). The SET process of the Pt/IGZO/IGZO:N/TiN device is described schematically in Fig. 9d (right). The higher N–O bonding energy of 201 kJ mol^{-1} compared to the O–O bonding energy of 146 kJ mol^{-1} allows nitrogen atoms to easily capture and concentrate oxygen ions around the CF tips.[172] This makes the IGZO:N layer act as an

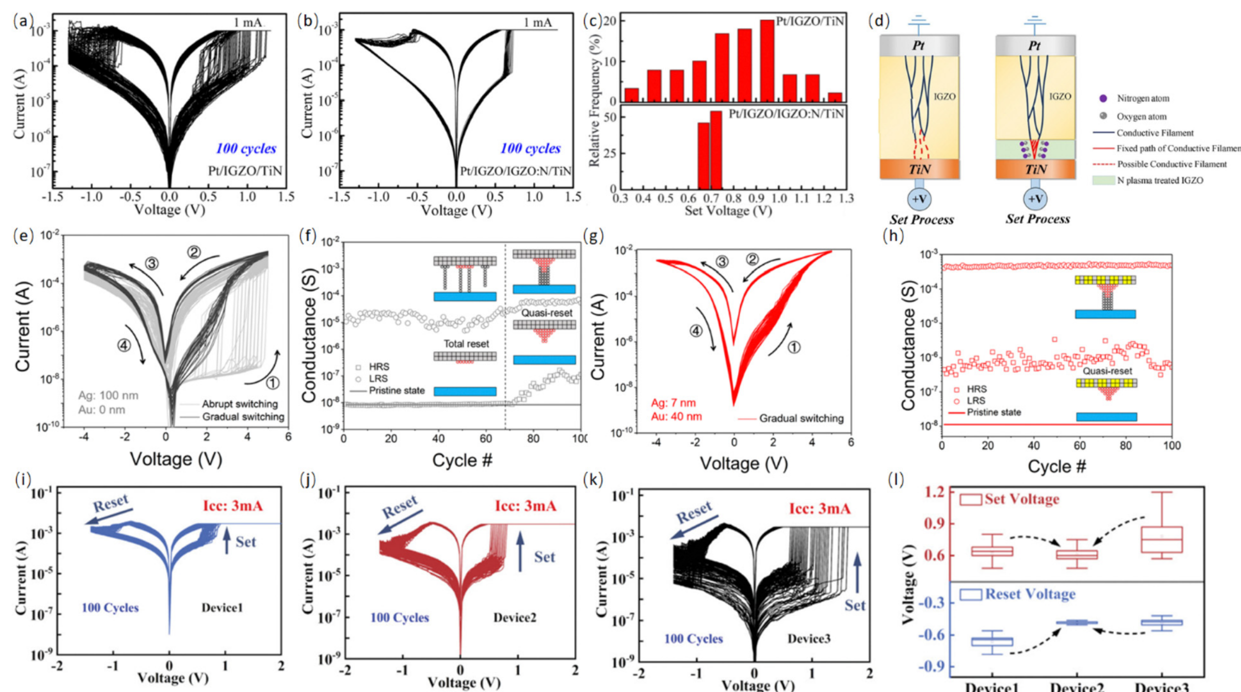

Fig. 9 Non-ideal variation in the memristor performance and enhancement strategies. IGZO-based memristors: *I–V* characteristics in the semi-log scale of (a) reference Pt/IGZO/TiN memristor and (b) plasma treated Pt/IGZO:N/TiN. (c) Associated SET voltages distribution for both memristors for a comparison. (d) Schematical illustration for switching mechanisms of both memristors and the effect of plasma treatment on performance variation. Reproduced with permission from ref. 169. Copyright 2020, Elsevier, native SiO_x based memristors: (e) *I–V* performance in the semi-log scale of a pure Ag/native SiO_x/p++-Si, (f) corresponding endurance characteristics with schematics of total RESET and Quasi-RESET. (g) *I–V* cycling of native SiO_x-based with Ag–Au composite TE and p++-Si BE. (h) Associated endurance with a schematic of the Quasi-RESET process. Reproduced with permission from ref. 171. Copyright 2022, American Chemical Society, and TaO_x-based memristors: *I–V* characteristics in the semi-log scale of (i) reference Ta/TaO_x/Pt memristor (Device1), (j) TaO_x-based memristor with a 2 nm Al_2O_3 inserting layer, that is Ta/TaO_x/2 nm Al_2O_3/Pt (Device2), and (k) Ta/TaO_x/4 nm Al_2O_3/Pt (Device3). (l) Corresponding distribution of SET and RESET voltages for all three memristors. The statistical distribution of the SET and RESET voltages is narrow for the memristor with the 2 nm Al_2O_3 inserting layer. Reproduced with permission from ref. 177. Copyright 2023, published by John Wiley and Sons. This is an open access article distributed under the terms of the Creative Commons CC BY license.

 © 2023 The Author(s). Published by the Royal Society of Chemistry

Open Access Article. Published on 31 ožujka 2023. Downloaded on 8.8.2024. 13:17:39.
This article is licensed under a Creative Commons Attribution-NonCommercial 3.0 Unported Licence.

oxygen reservoir,[169] enabling easier recombination between oxygen and oxygen vacancy and hence rupture of the conduction filaments (CFs), compared to the untreated Pt/IGZO/TiN device. The N atoms also help suppress the random formation of CFs, allowing the CF tips to grow along fixed paths in the IGZO:N layer, thereby improving the uniformity of set voltage distribution (*i.e.*, less variation).

Ma *et al.* reduced performance variation for a native SiO_x-based memristor by employing Ag–Au composite as top electrode.[171] In Fig. 9e and f, the memristor with single Ag as TE exhibits a sudden switching behavior with large variations in set voltages at the start of switching cycles (as shown in Fig. 9d with gray lines). This significant switching variation is mainly due to the formation of multiple delicate conductive filaments.[173,174] After a few switching cycles, the abrupt switching behavior of the device becomes uniform analog switching, as shown with black lines in Fig. 9e. This coincides with an increase in the conductance of HRS, as seen in Fig. 9f, which is indicative of a quasi-reset mode that is stabilized by residual (*i.e.*, incompletely ruptured) Ag. In their theoretical study, the presence of residual Ag is the main cause of variation improvement of resistive switching due to the depressed randomness of the conductive filament since residual Ag localizes the electric field.[175,176] To reduce the performance variation, the top electrode was redesigned: an Ag–Au composite was deposited on the native SiO_x layer, then the entire structure was capped with a pure Au layer. The *I–V* characteristics for the new design are displayed in Fig. 9g and h. Less variation is observed from the beginning of switching, *i.e.*, there is no transition from abrupt to analog switching. The active Ag in the Ag–Au composite is not continuous anymore because it is isolated by Au. The injection of Ag cations from the Ag–Au composite electrode is not widespread anymore, thus fewer but stronger Ag conductive filaments were formed during the initial set, resulting in a quasi-reset. This is further validated by the enhancement in retention characteristics.

Jiang *et al.* reported less variation of TaO_x-based memristor by inserting an Al_2O_3 layer between the switching layer and Pt bottom electrode.[177] The reference Ta/TaO_x/Pt memristor (Device1) was characterized by *I–V* sweeping and the result of 100 cycling is shown in Fig. 9i. Under the same testing condition, the characteristics of TaO_x-based memristors by inserting a 2 nm- (Device2) and 4 nm-thick (Device3) Al_2O_3 layer are displayed in Fig. 9j and k, respectively. From these *I–V* semi-log representations, Device2 has a higher on/off ratio and less variation than Device1. Device3 also has a high on/off ratio but appears more variation than Device1 and Device2. The statistics distribution of the SET and RESET voltages of the three devices in Fig. 9l present the variation differences in a quantitative way, confirming Device2 with a 2 nm inserting layer has the best performance in terms of variation. The authors proposed the following mechanisms behind the phenomena. The Al_2O_3 layer can be considered a limiting layer for the diffusion of oxygen ions.[177–180] Thus, the Al_2O_3 layer can be used to engineer the conductance modulation of the Ta/TaO_x/Al_2O_3/Pt memristor, by which the switching mechanism is modified and the DC sweeping characteristics are expected to be enhanced. Compared to the control memristor (*i.e.*, without the Al_2O_3 insertion layer), the oxygen ions along with the CFs are confined within the Al_2O_3 layer, leading to a quicker formation and disruption of the CFs.[177] However, employing a thicker inserting layer increased the variation. This could be due to the increased limiting effect of oxygen ion diffusion caused by a higher concentration of Al ions in the Al_2O_3 layer, leading to a more randomized connection and disconnection of the conductive filaments.[177] Therefore, optimization of the inserting layer's thickness is decisive as well.

11. Retention

Retention time is another technological merit to characterize the performance in terms of memristors' reliability.[177,181–188] The retention time is defined as, after the electrical bias is removed, the time duration that keeps each resistive state stable. Fig. 10a presents a comparison of retention time characteristics between an early failed reference sample-1 (Pt/HfO_x/Ti memristor) and a long retention sample-3.[189] The current level of sample-1 was read with 0.1 V every 5 seconds at 85 °C. After 100 s, the resistive states changed abruptly (*i.e.*, resistance dropped), indicating the storage information in the memristor was lost. With modified bottom electrode Ti by polydopamine (PDA)/Ag nanoparticles (AgNPs), sample-3's HRS and LRS last 10^4 s under the same measurement conditions. The longer retention time of sample-3 was ascribed to the local electrical field enhancement of AgNPs. It is widely accepted that the memristor should have 10 years of retention time at 85 °C for practical applications, and such long-time testing is not realistic, so the data are extrapolated to get an estimation. In Fig. 10b, the data from retention test of a Cu/α-Si (amorphous Si)/α-C (amorphous C)/Pt device in a memristor crossbar array at 100 °C is displayed.[190] The resistive states kept stable for more than 10^5 s and the data's extrapolation reached 10 years of retention time approximately. The mechanism of retention was related to the conductive filament's rupture. Im *et al.* enhanced the retention time of Halide perovskites (HPs) based memristors by modulating the Ag doping concentration and suggested related mechanisms.[191] There is a persistent tendency for the conductive filament to diffuse out, and so its conductive network is broken down. This is caused by the chemical potential gradient at the filament's surface and the desire to minimize its surface energy.[191–195] Based on the Gibbs–Thomson effect, the surface atomic flux (J_s) on the filament surface determines the lifespan of conductive filament, and J_s strongly depends on the filament's radius.[191,195] The larger radius yields a slower surface diffusion. Fig. 10c shows that the retention time changes with the Ag concentrations in $CH_3NH_3PbI_3$ ($MAPbI_3$):Ag-based memristors. A transition from volatile threshold switching (temporary switching) to non-volatile resistive switching was observed. With a rise in the Ag doping concentration, there was a corresponding increase in retention time. The mechanisms of threshold,

Open Access Article. Published on 31 ožujka 2023. Downloaded on 8.8.2024. 13:17:39.
This article is licensed under a Creative Commons Attribution-NonCommercial 3.0 Unported Licence.

Fig. 10 Representative retention behaviors of memristors. (a) Retention characteristics at 85 °C of sample-1 Pt/HfO_x/Ti and sample-3 PDA/AgNPs modified TE memristors. Reproduced with permission from ref. 189. Copyright 2021, AIP Publishing, (b) retention measurement on Cu/α-Si/α-C/Pt memristor at 100 °C, and the extrapolated retention, reaching 10 years of retention. Reproduced with permission from ref. 190. Copyright 2022, published by John Wiley and Sons. This is an open access article distributed under the terms of the Creative Commons CC BY license, $MAPbI_3$:Ag-based memristors: (c) the relationship between retention time and the Ag doping concentration. (d) The schematic of the mechanisms of the threshold and resistive switching. Reproduced with permission from ref. 191. Copyright 2022, John Wiley and Sons, Superlattice-like (SLL) structure memristors: (e) the design of Ti/(HfO_x/AlO_y)SLL/TiN memristor, where yellow colored layers are AlO_y and layers with light blue represent HfO_x. (f) At 85 °C, retention characteristics of eight conductance levels. Reproduced with permission from ref. 196. Copyright 2022, published by John Wiley and Sons. This is an open access article distributed under the terms of the Creative Commons CC BY license, and Nanosheets CIS-based memristor: (g) structure of memristive arrays with Au top electrodes. (h) Top view SEM image of the CIS nanosheets layer. Reproduced with permission from ref. 197. Copyright 2023, The Royal Society of Chemistry.

resistive switching, and transition were proposed in Fig. 10d. Low Ag concentration devices induce weak filaments with a smaller radius due to the limited Ag concentration. As discussed previously, a smaller radius of filaments leads to larger J_s, *i.e.*, faster surface diffusion.[191,195] Thus, the removal of the external field annihilates the weak filaments, resulting in a shorter retention time. In a similar way, the higher Ag doping concentration prolonged lifetime of the filament by slowing down the diffusion. It is desirable to achieve multiple conductance states with long retention time, especially for neuromorphic computing, which may require additional components in the device structure (*i.e.*, changing device structure).

Wang *et al.* demonstrated a superlattice-like (SLL) structure memristor (Fig. 10e) by incorporating several layers of alternating AlO_y (yellow) with the HfO_x functioning layer.[196] Under the test condition of 100 mV read voltage and 1 second read interval at 85 °C, Fig. 10f shows that eight conductance states remained stable for more than 10^4 s without considerable drift. Adding several AlO_y barrier layers to the HfO_x switching layer reduced the strength of the Vo conductive filament, by which the formation and rupture process becomes gradual. Then, multiple states were achieved because oxygen ions must continuously pass through the barrier layers when exposed to successive pulses of limited energy during the migration

 © 2023 The Author(s). Published by the Royal Society of Chemistry

process. Besides the barriers, Hf–O–Al bond on oxygen atoms triggered the confinement effect, thus, the relaxation of the conductive filament was controllable. Another method for improving retention characteristics is to change the morphology of the switching layer. Hu *et al.* used unique vertical nanosheet $CuInS_2$ (CIS) arrays featuring nanoscale pores rather than conventional CIS film as the functioning layer (Fig. 10g).[197] Fig. 10h is the top view high-magnification SEM image of the CIS nanosheets layer. The retention time for nanosheets CIS-based memristor was reported as much enhanced 10^4 s, compared to that of the conventional film-based memristor. The enhancement was attributed to the network-limited vertical structure and efficient isolation of leakage paths by the demonstrated porous structure.

12. Linearity

In the section on image processing, we reviewed a neural network implemented by a memristive crossbar for *in situ* backpropagation training. One of the key takeaways that we gleaned from that characterization method is that synaptic weight was denoted as memristor's conductance (G), and it was modulated continuously during the training. In a view of the single device level, this kind of modulation can be considered as that memristor mimics the long synaptic plasticity including long-term potentiation (LTP) and long-term depression (LTD). The LTP process increases the conductance of the memristor and LTD decreases it. These processes are induced by applying the opposite bias of the pulse train and visualized in Fig. 11a with an inset image of a memristive crossbar.[198] It is preferable to tune the memristor in a linear and symmetric manner, ensuring that every electrical stimulus (*e.g.*, pulse count or width) elicits an equal update of conductance during both potentiation (SET) and depression (RESET) transitions.[199] However, in reality, the LTP and LTD processes are plagued by non-linearity and asymmetry issues from the conductance modulation. The symptoms of these issues were summarized in Fig. 11b. By applying identical pulses (*i.e.*, same duration and the same amplitude, but opposite directions for the two train), the red line symbolizes the ideal correspondence between conductance and the number of pulses, and the black curve portrays the one for an actual memristor device. In a LTP process, for a scenario where the conductance of a memristor is required to be increased from *a* to *b*, the ideal linear function is usually used to calculate the needed pulse stimuli.[198] Yet, upon application of the calculated pulses to the actual memristor, the conductance deviates from its expected trajectory and shifts from point *a* to *c* instead of from point *a* to *b*. A comparable error in weight updating happens during the LTD process. As a result, the actual updates in conductance and the desired change are vastly disparate due to the nonlinearity issue, which subsequently diminishes the accuracy of the neural network computing. One alternate mechanism behind the nonlinearity issue is the presence of two phases in the evolution process of the conductive filament.[200] Using the creation of the filament as an illustration, the first stage involves the growth of the conductive filament until it connects the bottom and top electrode, which is regulated by the drift of metallic ions or oxygen vacanccies[200–202] Once the filament is formed, it tends to further thicken by ion diffusions.[200,202–204]

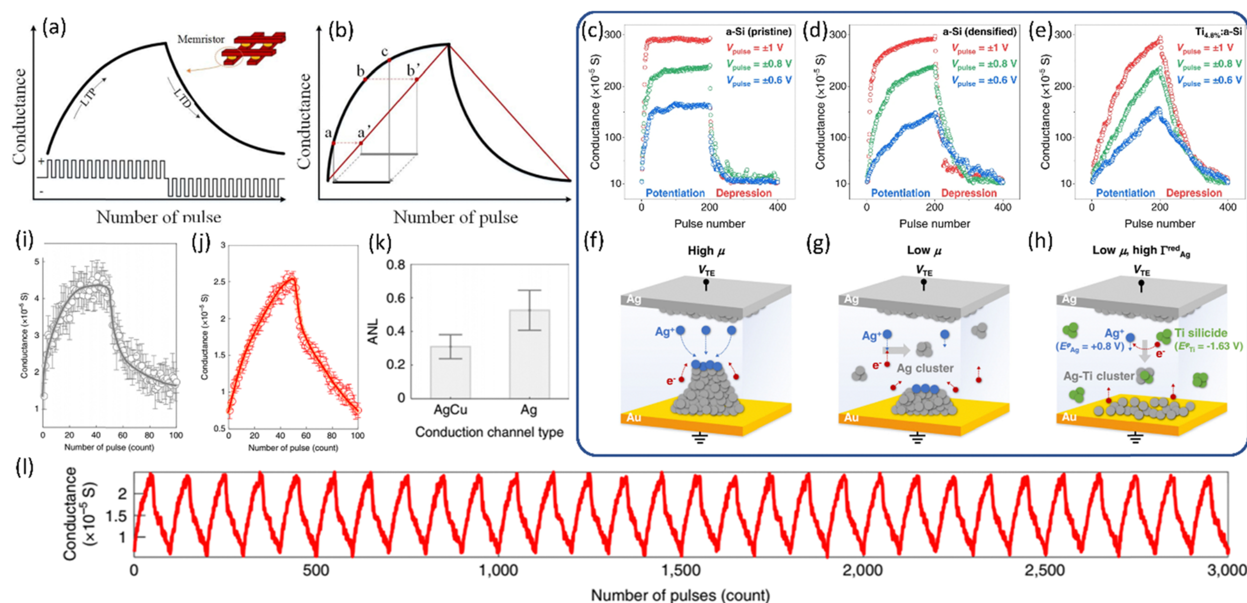

Fig. 11 Demonstration of synaptic weight updating process: (a) conductance changes by applying identical pulses (b) weight updating process based on ideal linearity. Reproduced with permission from ref. 198. Copyright 2019, IEEE, synaptic weight updating performance and mechanisms on memristors with the switching layer of (c and f) low-density a-Si, (d and g) densified a-Si, and (e and h) Ti nanoclusters embedded densified a-Si. Reproduced with permission from ref. 209. Copyright 2022, Springer Nature, and conductance changes of Si-based memristor by applying nanosecond scale pulses with (i) Ag only top electrode and (j) Ag–Cu alloying one. (k) Associated statistics report on ANL of these two kinds of memristors. (l) 30-Cycle conductance programming of AgCu alloying memristor. Reproduced with permission from ref. 210. Copyright 2020, Springer Nature.

Open Access Article. Published on 31 ožujka 2023. Downloaded on 8.8.2024. 13:17:39. This article is licensed under a Creative Commons Attribution-NonCommercial 3.0 Unported Licence.

Open Access Article. Published on 31 ožujka 2023. Downloaded on 8.8.2024. 13:17:39.
This article is licensed under a Creative Commons Attribution-NonCommercial 3.0 Unported Licence.

The strategies such as material engineering have been employed to attain desirable linearity.[205–208] Kang *et al.* achieved an improved linearity of amorphous Si (a-Si)-based memristors through densification of the switching layer a-Si.[209] The linearity was further enhanced by the inclusion of Ti nanoclusters. Fig. 11c shows the a-Si-based memristor suffered a non-linearity issue, under three different amplitudes of pulses and a filamentary mechanism is illustrated in Fig. 11f. They claimed that the relatively low density of a-Si leads to high cation mobility, thus the injected Ag ions rapidly arrive at the bottom electrode and reduce and accumulate there. Consequently, the filament that grows from the bottom experiences strong reinforcement from the local electric field, resulting in a non-linear issue. So, a densified a-Si memristor was fabricated to slow the ions' migration so that the Ag-clusters are formed inside the a-Si to reduce the buildup of silver (Fig. 11g). Its performance was plotted in Fig. 11d and the improvements on linearity were observed, especially with low amplitudes of pulses. The large dynamic range, *i.e.*, on/off ratio, is important to memristors, thus, the linearity with high pulse amplitudes should continue to be optimized. They introduced Ti nanoclusters with negative reduction potential to capture and reduce the migrating Ag cations to Ag-clusters (Fig. 11h). The linearity results summarized in Fig. 11e manifest the enhancements with all three pulse amplitudes due to the increased reduction probability of Ag cations inside the a-Si switching layer. The quantitative evaluation method for linearity was clearly described in this work as well. Yeon *et al.* demonstrated that alloying top electrode helps alleviate the nonlinearity issue.[210] Fig. 11i is a linearity examination for a Si-based memristor with a commonly used Ag top electrode, and shows a sudden drop of conductance, indicating a nonlinearity issue. With the Ag–Cu alloying, a more linear and symmetric switching was achieved (Fig. 11j) and the asymmetric non-linearity factor (ANL) was calculated to characterize the improvement which drops to an average value from 0.59 to 0.3 with Ag only devices (Fig. 11k). They speculated the alloying yields a stabilized interaction of conduction channels to refine the performance of conductance updating. 30 cycles of LTP/LTD on Ag–Cu alloying memristor were measured by using nanosecond scale width for the pulses and associated results were displayed in Fig. 11l. Engineering pulsing scheme may also address the nonlinearity challenge;[211,212] however, the linearity and symmetry problems need to be more fundamentally mitigated by engineering materials structures and properties, and the associated device architecture.[200]

Part III. Theoretical calculations

13. Density functional theory (DFT) and molecular dynamics (MD) simulations

Density functional theory (DFT) and molecular dynamics (MD) simulations are extensively leveraged to study the electronic structure of materials and the dynamic behavior of atoms and molecules, which is often difficult to be identified with macroscale characterizations, in the fields of physics, chemistry, and materials science.[213–216] Regarding memristors, these simulation methods are commonly employed to investigate the switching mechanisms, assist in device design, and provide support for experimental findings.[217–223]

Zhu *et al.* optimized the amorphous HfO_2 (a-HfO_2)-based memristor performance with an additional Al-doped HfO_2 layer (*i.e.*, bilayer structure).[224] The Pt/HfO_2:Al/HfO_2/TiN memristor demonstrated enhanced cycling endurance and less cycle-to-cycle variation. DFT simulation was employed to study the properties of the HfO_2:Al layer which provided a foundation to explain the switching mechanism and the underlying reasons for the enhancements. Fig. 12a displays the statistical distribution of the calculated formation energies of V_O in a-HfO_2 and a-HfO_2:Al, which were calculated at ten different positions within the considered unit cell of the two cases, reflecting the disordered states of amorphous materials (*i.e.*, HfO_2). In a-HfO_2, the average V_O formation energy is approximately 6.24 eV, whereas in a-HfO_2:Al, it is 3.29 eV, indicating that V_O is more easily generated with the incorporation of Al. Fig. 12b and c illustrate the diffusion barrier profiles of V_O migration in a-HfO_2 and a-HfO_2:Al, simulated by relocating the oxygen atom from its original site to neighboring vacancies. The migration barrier of V_O in a-HfO_2 is 2.72 eV, compared to 2.21 eV in a-HfO_2:Al, indicating that V_O can migrate more easily in a-HfO_2:Al. Consequently, the V_O CF is likely to have a greater preference for growth in a-HfO_2:Al.

Goul *et al.* reported tunable on/off ratio Al_2O_3-based memristors guided by their DFT simulation results.[225] Fig. 12d displays the computed defect formation energy plotted against the Fermi level location. The graph showcases the results for native defects, such as V_O, aluminum vacancy (V_{Al}), and aluminum interstitial (Al_i), and defects from Mg doping, including Mg substituting on Al (Mg_{Al}), Mg substituting on Al (Mg_O), and Mg interstitials (Mg_i) under both Al-rich and O-rich conditions. By introducing Mg in the DFT calculation, the anticipated position of the Fermi level will relocate towards the valence band maximum, as indicated by the arrows and solid vertical lines in Fig. 12d. This downward Fermi level shift yields two benefits for improving the performance of Al_2O_3-based memristors: firstly, a reduced Fermi level implies greater insulation/resistance in the HRS of Mg-doped Al_2O_3. Secondly, at these lower Fermi levels, the formation energy of V_O is decreased, indicating that a greater number of V_O will form. Following the DFT calculations, interfacial MgO layer(s) as the method of Mg doping is implemented in the Al_2O_3 switching layer to engineer the switching performance of Al_2O_3-based memristors.

Onofrio *et al.* simulated ECM switching behaviors in a SiO_2-based memristor by the MD method.[226] The active electrode was Cu and its surface was designed with triangular or conical patterns to emulate the unevenness, typically observed in actual samples. Fig. 12e depicts the cell's resistance state over time as a result of the simulation, while Fig. 12f–i exhibit atomic snapshots capturing crucial stages of the process. Applying the initial forming voltage causes the Cu atoms near the active

 © 2023 The Author(s). Published by the Royal Society of Chemistry

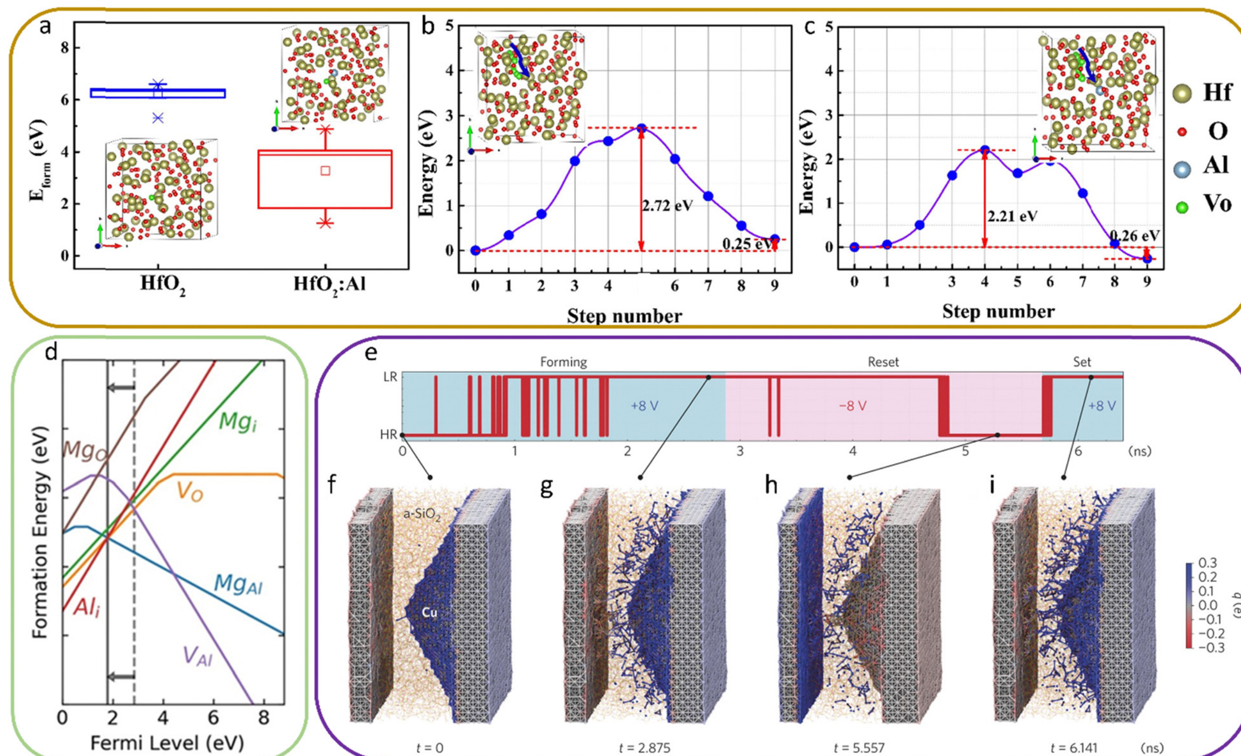

Fig. 12 DFT and MD simulations for device design and mechanism exploration. DFT simulations for aHfO_2-based memristors with Pt TE and TiN BE: (a) the formation energy distribution of oxygen vacancies in a-HfO_2 and a-HfO_2:Al. The insets display the a-HfO_2 and a-HfO_2:Al structures with a V_O. Reproduced with permission from ref. 224. Copyright 2021, Elsevier, DFT simulations for Al_2O_3-based memristors with Pd TE and Al BE: (d) The defect formation energy of native and Mg-related defects in Al_2O_3 as a function of the Fermi level. Reproduced with permission from ref. 225. Copyright 2022, Springer Nature, MD simulations for SiO_2-based memristors: (e) the scale indicates how the SiO_2-based memristor switches on and off in response to the simulation time. The evolution of atomic structure and charge states is represented at (f) initial HRS, (g) forming LRS, (h) HRS, and (i) SET LRS. Reproduced with permission from ref. 226. Copyright 2015, Springer Nature.

Open Access Article. Published on 31 ožujka 2023. Downloaded on 8.8.2024. 13:17:39.
This article is licensed under a Creative Commons Attribution-NonCommercial 3.0 Unported Licence.

electrode's surface to become positively charged (blue atoms in Fig. 12f), which increases their likelihood of dissolving into the SiO_2 electrolyte. Within one nanosecond, the simulations indicate that these dissolved atoms form the first bridging filaments. Interestingly, these early connections are short-lived, unstable states consisting of a single-atom chain, and the device switches back and forth between the on and off states for another nanosecond until a stable filament is formed. The snapshots in Fig. 12g display the stable nanofilament that bridges the electrodes, along with other partially grown filaments linked to the inactive electrode. With a negative bias, the filament fractures near the inactive electrode, leaving behind an incomplete filament that is now attached to the active electrode (refer to Fig. 12h). After the RESET, applying a positive bias quickly creates a new connection (shown in Fig. 12i), effectively turning the device back on. The MD simulations offer a detailed view of the operational mechanisms at an atomic level, and with a superior time resolution.

In summary of this section, DFT and MD simulations are effective methods for studying the formation energy of defects, the energy barriers of ion migration, and the dynamics of resistive switching at the atomic level, which will be valuable supplements to instrumental characterizations.

14. Conclusions and perspectives

This review comprehensively focuses on the two main aspects of memristors and their potential energy-efficient neuromorphic computing. As one of the focused topics of characterizations for memristor materials and devices, structure, chemical and electronic evaluation techniques such as TEM, XPS, and AFM are of crucial importance to examining the device structure, identifying the switching mechanisms, and engineering the switching layer (*e.g.*, composition and dimension). Figures of merit performance of memristor devices are generally determined by various electrical measurements. DC sweeping provides a variety of fundamental characteristics, including bipolar switching behavior, on/off ratio, endurance, and conduction mechanism. Pulse measurements are another instrumental electrical characterization method to evaluate endurance behaviors in a way closer to practical application while linearity needs to be considered for neural network establishment. Advanced image processing is a characterization method to evaluate analog tuning accuracy. CV and EIS are widely used in electrochemical research, and they are also introduced for exploring the selection criterion of electrode materials and switching mechanisms of memristors.

Open Access Article. Published on 31 ožujka 2023. Downloaded on 8.8.2024. 13:17:39.
This article is licensed under a Creative Commons Attribution-NonCommercial 3.0 Unported Licence.

As another main subject, the reliability of memristors is typically evaluated by four criteria including endurance, variation, retention, and linearity. Each of these reliability issues is discussed in-depth and corresponding characteristics indicators, mechanisms, and measurement standards are provided and elaborated. Possible mitigation approaches to these reliability concerns are suggested as well. DFT and MD simulations play an important role in the design process, aiding in the interpretation of experimental results and facilitating an understanding of switching behaviors.

The memristor has been theoretically proposed for more than forty years, and experimental efforts have been made actively for more than a decade. However, some of the fundamentals stay controversial, and the commercial adoption of memristors is still hindered due to the lack of these fundamentals and reliability issues. Further endeavors must be pursued to rectify these limitations. Besides applying memristors to numerous applications, it is urgent to objectively report the characteristics, clarify the key issues of various non-ideal performance and identify the underlying mechanisms. Researchers from diverse fields still possess a remarkable opportunity to drive the progression of memristors by further establishing the switching/failure mechanisms with both typical and novel characterization techniques. In addition, strategic designs of materials and devices can address multiple reliability concerns simultaneously. For instance, as demonstrated in Yeon *et al.*'s study reviewed in the linearity section, the Ag–Cu electrode alloying significantly improved both the variation and retention as well at the single device level, which in turn leads to reliable crossbar arrays.[210] Also, as this example shows, the improvements in crossbar performance frequently stem from single-device level optimization, thus, the examination at the single-device level remains crucial and is still highly recommended in this field. Meanwhile, with booming neuromorphic applications, materials researchers should acquire knowledge of neural networks to address the issues at a single-device level and synergistically collaborate with data science and circuit engineers for practical computing applications. We believe that advancing the characterization methods will continue enhancing the memristor's fundamentals and understanding the reliability issues constitutes a vital step towards optimizing the functioning of the memristor.

Conflicts of interest

There are no conflicts to declare.

Acknowledgements

This work was supported by the U.S. National Science Foundation (NSF) Awards ECCS-1931088 and CBET-2207302. S. L. and H. W. S. acknowledge the support from the Improvement of Measurement Standards and Technology for Mechanical Metrology (Grant No. 23011043) by KRISS. The authors would like to thank Xingyu Fu and Fengfeng Zhou for the constructive discussion on Image processing.

References

1 L. Chua, *IEEE Trans. Circuit Theory*, 1971, **18**, 507–519.
2 J. J. Yang, M. D. Pickett, X. Li, D. A. A. Ohlberg, D. R. Stewart and R. S. Williams, *Nat. Nanotechnol.*, 2008, **3**, 429–433.
3 D. B. Strukov, G. S. Snider, D. R. Stewart and R. S. Williams, *Nature*, 2008, **453**, 80–83.
4 D. B. Strukov, G. S. Snider, D. R. Stewart and R. S. Williams, *Nature*, 2009, **459**, 1154.
5 N. D. Mathur, *Nature*, 2008, **455**, E13.
6 J. J. Yang, M. X. Zhang, J. P. Strachan, F. Miao, M. D. Pickett, R. D. Kelley, G. Medeiros-Ribeiro and R. S. Williams, *Appl. Phys. Lett.*, 2010, **97**, 3–5.
7 X. Li, H. Wu, G. Bin, W. Wu, D. Wu, N. Deng, J. Cai and H. Qian, *Nanotechnology*, 2016, **27**, 305201.
8 Y.-E. Syu, T.-C. Chang, J.-H. Lou, T.-M. Tsai, K.-C. Chang, M.-J. Tsai, Y.-L. Wang, M. Liu and S. M. Sze, *Appl. Phys. Lett.*, 2013, **102**, 172903.
9 Z. Fang, H. Y. Yu, W. J. Liu, Z. R. Wang, X. A. Tran, B. Gao and J. F. Kang, *IEEE Electron Device Lett.*, 2010, **31**, 476–478.
10 S. U. Sharath, S. Vogel, L. Molina-Luna, E. Hildebrandt, C. Wenger, J. Kurian, M. Duerrschnabel, T. Niermann, G. Niu, P. Calka, M. Lehmann, H.-J. Kleebe, T. Schroeder and L. Alff, *Adv. Funct. Mater.*, 2017, **27**, 1700432.
11 C. H. Kim, Y. H. Jang, H. J. Hwang, C. H. Song, Y. S. Yang and J. H. Cho, *Appl. Phys. Lett.*, 2010, **97**, 1–3.
12 M. C. Chen, T. C. Chang, S. Y. Huang, S. C. Chen, C. W. Hu, C. T. Tsai and S. M. Sze, *Electrochem. Solid-State Lett.*, 2010, **13**, 191–194.
13 Z. Q. Wang, H. Y. Xu, X. H. Li, X. T. Zhang, Y. X. Liu and Y. C. Liu, *IEEE Electron Device Lett.*, 2011, **32**, 1442–1444.
14 Z. Q. Wang, H. Y. Xu, X. H. Li, H. Yu, Y. C. Liu and X. J. Zhu, *Adv. Funct. Mater.*, 2012, **22**, 2759–2765.
15 M. S. Kim, Y. Hwan Hwang, S. Kim, Z. Guo, D. I. Moon, J. M. Choi, M. L. Seol, B. S. Bae and Y. K. Choi, *Appl. Phys. Lett.*, 2012, **101**, 3–6.
16 Y. S. Fan, P. T. Liu and C. H. Hsu, *Thin Solid Films*, 2013, **549**, 54–58.
17 Y. H. Hwang, H. M. An and W. J. Cho, *Jpn. J. Appl. Phys.*, 2014, **53**, 1–4.
18 Y. Pei, B. Mai, X. Zhang, R. Hu, Y. Li, Z. Chen, B. Fan, J. Liang and G. Wang, *J. Electron. Mater.*, 2015, **44**, 645–650.
19 C. C. Lo and T. E. Hsieh, *J. Phys. D: Appl. Phys.*, 2016, **49**, 385102.
20 Q. Li, Y. Li, L. Gao, F. Ma, Z. Song and K. Xu, *RSC Adv.*, 2016, **6**, 42347–42352.
21 F. Qin, Y. Zhang, H. Park, C. S. Kim, D. H. Lee, Z.-T. Jiang, J. Park, K. No, H. Park, H. W. Song and S. Lee, *Phys. Status Solidi RRL*, 2022, **16**, 2200075.
22 M. A. Zidan, H. A. H. Fahmy, M. M. Hussain and K. N. Salama, *Microelectron. J.*, 2013, **44**, 176–183.

© 2023 The Author(s). Published by the Royal Society of Chemistry

Open Access Article. Published on 31 ožujka 2023. Downloaded on 8.8.2024. 13:17:39.
This article is licensed under a Creative Commons Attribution-NonCommercial 3.0 Unported Licence.

23 T. You, N. Du, S. Slesazeck, T. Mikolajick, G. Li, D. Bürger, I. Skorupa, H. Stöcker, B. Abendroth, A. Beyer, K. Volz, O. G. Schmidt and H. Schmidt, *ACS Appl. Mater. Interfaces*, 2014, **6**, 19758–19765.

24 H. Jeong and L. Shi, *J. Phys. D: Appl. Phys.*, 2019, **52**, 023003.

25 W. Q. Pan, J. Chen, R. Kuang, Y. Li, Y. H. He, G. R. Feng, N. Duan, T. C. Chang and X. S. Miao, *IEEE Trans. Electron Devices*, 2020, **67**, 895–901.

26 K. Sun, J. Chen and X. Yan, *Adv. Funct. Mater.*, 2021, **31**, 1–33.

27 H. Kim, M. P. Sah, C. Yang, T. Roska and L. O. Chua, *Proc. IEEE*, 2012, **100**, 2061–2070.

28 S. H. Jo, T. Chang, I. Ebong, B. B. Bhadviya, P. Mazumder and W. Lu, *Nano Lett.*, 2010, **10**, 1297–1301.

29 D. V. Christensen, R. Dittmann, B. Linares-Barranco, A. Sebastian, M. Le Gallo, A. Redaelli, S. Slesazeck, T. Mikolajick, S. Spiga, S. Menzel, I. Valov, G. Milano, C. Ricciardi, S.-J. Liang, F. Miao, M. Lanza, T. J. Quill, S. T. Keene, A. Salleo, J. Grollier, D. Marković, A. Mizrahi, P. Yao, J. J. Yang, G. Indiveri, J. P. Strachan, S. Datta, E. Vianello, A. Valentian, J. Feldmann, X. Li, W. H. P. Pernice, H. Bhaskaran, S. Furber, E. Neftci, F. Scherr, W. Maass, S. Ramaswamy, J. Tapson, P. Panda, Y. Kim, G. Tanaka, S. Thorpe, C. Bartolozzi, T. A. Cleland, C. Posch, S. Liu, G. Panuccio, M. Mahmud, A. N. Mazumder, M. Hosseini, T. Mohsenin, E. Donati, S. Tolu, R. Galeazzi, M. E. Christensen, S. Holm, D. Ielmini and N. Pryds, *Neuromorphic Comput. Eng.*, 2022, **2**, 022501.

30 C. Sung, H. Hwang and I. K. Yoo, *J. Appl. Phys.*, 2018, **124**, 151903.

31 H. Jiang, D. Belkin, S. E. Savel'Ev, S. Lin, Z. Wang, Y. Li, S. Joshi, R. Midya, C. Li, M. Rao, M. Barnell, Q. Wu, J. J. Yang and Q. Xia, *Nat. Commun.*, 2017, **8**, 882.

32 Q. Liu, J. Sun, H. Lv, S. Long, K. Yin, N. Wan, Y. Li, L. Sun and M. Liu, *Adv. Mater.*, 2012, **24**, 1844–1849.

33 J. Y. Chen, C. W. Huang, C. H. Chiu, Y. T. Huang and W. W. Wu, *Adv. Mater.*, 2015, **27**, 5028–5033.

34 F. Yuan, Z. Zhang, C. Liu, F. Zhou, H. M. Yau, W. Lu, X. Qiu, H. S. P. Wong, J. Dai and Y. Chai, *ACS Nano*, 2017, **11**, 4097–4104.

35 Z. Wang, S. Joshi, S. E. Savel'ev, H. Jiang, R. Midya, P. Lin, M. Hu, N. Ge, J. P. Strachan, Z. Li, Q. Wu, M. Barnell, G.-L. Li, H. L. Xin, R. S. Williams, Q. Xia and J. J. Yang, *Nat. Mater.*, 2017, **16**, 101–108.

36 J. Yin, F. Zeng, Q. Wan, F. Li, Y. Sun, Y. Hu, J. Liu, G. Li and F. Pan, *Adv. Funct. Mater.*, 2018, **28**, 1706927.

37 X. Yan, J. Zhao, S. Liu, Z. Zhou, Q. Liu, J. Chen and X. Y. Liu, *Adv. Funct. Mater.*, 2018, **28**, 1705320.

38 I. Zrinski, C. C. Mardare, L.-I. Jinga, J. P. Kollender, G. Socol, A. Minenkov, A. W. Hassel and A. I. Mardare, *Nanomaterials*, 2021, **11**, 666.

39 Y. R. Park, H. Cho and G. Wang, *ACS Appl. Electron. Mater.*, 2022, **4**, 3739–3748.

40 S.-J. Choi, G.-S. Park, K.-H. Kim, S. Cho, W.-Y. Yang, X.-S. Li, J.-H. Moon, K.-J. Lee and K. Kim, *Adv. Mater.*, 2011, **23**, 3272–3277.

41 T. Fujii, M. Arita, Y. Takahashi and I. Fujiwara, *Appl. Phys. Lett.*, 2011, **98**, 212104.

42 G.-S. Park, Y. B. Kim, S. Y. Park, X. S. Li, S. Heo, M.-J. Lee, M. Chang, J. H. Kwon, M. Kim, U. I. Chung, R. Dittmann, R. Waser and K. Kim, *Nat. Commun.*, 2013, **4**, 2382.

43 Y. Li, Z. Wang, R. Midya, Q. Xia and J. J. Yang, *J. Phys. D: Appl. Phys.*, 2018, **51**, 503002.

44 Y. Li, L. Loh, S. Li, L. Chen, B. Li, M. Bosman and K.-W. Ang, *Nat. Electron.*, 2021, **4**, 348–356.

45 Y. Yang, P. Gao, S. Gaba, T. Chang, X. Pan and W. Lu, *Nat. Commun.*, 2012, **3**, 732.

46 Y. Zhang, G.-Q. Mao, X. Zhao, Y. Li, M. Zhang, Z. Wu, W. Wu, H. Sun, Y. Guo, L. Wang, X. Zhang, Q. Liu, H. Lv, K.-H. Xue, G. Xu, X. Miao, S. Long and M. Liu, *Nat. Commun.*, 2021, **12**, 7232.

47 S. H. Jo and W. Lu, *Nano Lett.*, 2008, **8**, 392–397.

48 R. Waser and M. Aono, *Nat. Mater.*, 2007, **6**, 833–840.

49 R. Waser, R. Dittmann, G. Staikov and K. Szot, *Adv. Mater.*, 2009, **21**, 2632–2663.

50 J. H. Yoon, J. Zhang, P. Lin, N. Upadhyay, P. Yan, Y. Liu, Q. Xia and J. J. Yang, *Adv. Mater.*, 2020, **32**, 1–9.

51 H. Huang, Y. Qiao, Y. Yuan and J. Zhang, *Reference Module in Materials Science and Materials Engineering*, Elsevier, 2022, DOI: 10.1016/B978-0-12-822425-0.00073-7.

52 R. R. Mather, in *Surface Modification of Textiles*, ed. Q. Wei, Woodhead Publishing, 2009, pp. 296–317, DOI: 10.1533/9781845696689.296.

53 M. K. Rahmani, M. Ismail, C. Mahata and S. Kim, *Results Phys.*, 2020, **18**, 103325.

54 S. Kim, H. Kim, S. Hwang, M.-H. Kim, Y.-F. Chang and B.-G. Park, *ACS Appl. Mater. Interfaces*, 2017, **9**, 40420–40427.

55 F. Miao, W. Yi, I. Goldfarb, J. J. Yang, M.-X. Zhang, M. D. Pickett, J. P. Strachan, G. Medeiros-Ribeiro and R. S. Williams, *ACS Nano*, 2012, **6**, 2312–2318.

56 T.-Y. Wang, J.-L. Meng, M.-Y. Rao, Z.-Y. He, L. Chen, H. Zhu, Q.-Q. Sun, S.-J. Ding, W.-Z. Bao, P. Zhou and D. W. Zhang, *Nano Lett.*, 2020, **20**, 4111–4120.

57 X. Shan, C. Zhao, X. Wang, Z. Wang, S. Fu, Y. Lin, T. Zeng, X. Zhao, H. Xu, X. Zhang and Y. Liu, *Adv. Sci.*, 2022, **9**, 2104632.

58 O. Kapur, D. Guo, J. Reynolds, Y. Han, R. Beanland, L. Jiang, C. H. de Groot and R. Huang, *Adv. Electron. Mater.*, 2022, **8**, 2200312.

59 Y. Lee, C. Mahata, M. Kang and S. Kim, *Appl. Surf. Sci.*, 2021, **565**, 150563.

60 P. Cheng, K. Sun and Y. H. Hu, *Nano Lett.*, 2016, **16**, 572–576.

61 J. Park, E. Park and H.-Y. Yu, *Appl. Surf. Sci.*, 2022, **603**, 154307.

62 Z. Wang, L. Wang, Y. Wu, L. Bian, M. Nagai, R. Jv, L. Xie, H. Ling, Q. Li, H. Bian, M. Yi, N. Shi, X. Liu and W. Huang, *Adv. Mater.*, 2021, **33**, 2104370.

63 I. Köymen, P. Aydoğan Göktürk, C. Kocabaş and Ş. Süzer, *Faraday Discuss.*, 2019, **213**, 231–244.

64 Y. S. Kim, J. An, J. B. Jeon, M. W. Son, S. Son, W. Park, Y. Lee, J. Park, G. Y. Kim, G. Kim, H. Song and K. M. Kim, *Adv. Sci.*, 2022, **9**, 1–9.

65 X. Shi, W. Qing, T. Marhaba and W. Zhang, *Electrochim. Acta*, 2020, **332**, 135472.

Open Access Article. Published on 31 ožujka 2023. Downloaded on 8.8.2024. 13:17:39.
This article is licensed under a Creative Commons Attribution-NonCommercial 3.0 Unported Licence.

66 H. Assender, V. Bliznyuk and K. Porfyrakis, *Science*, 2002, **297**, 973–976.

67 H.-J. Butt, B. Cappella and M. Kappl, *Surf. Sci. Rep.*, 2005, **59**, 1–152.

68 M. Rief, M. Gautel, F. Oesterhelt, J. M. Fernandez and H. E. Gaub, *Science*, 1997, **276**, 1109–1112.

69 J. W. Suk, R. D. Piner, J. An and R. S. Ruoff, *ACS Nano*, 2010, **4**, 6557–6564.

70 C. Villeneuve-Faure, K. Makasheva, L. Boudou and G. Teyssedre, *Nanotechnology*, 2016, **27**, 245702.

71 P. K. Ingram, G. J. Wilson and R. Devonshire, *Appl. Surf. Sci.*, 1999, **146**, 363–370.

72 K. Mahankali, N. K. Thangavel and L. M. Reddy Arava, *Nano Lett.*, 2019, **19**, 5229–5236.

73 S. Kim, Y. Lee, M. Lee, S. An and S.-J. Cho, *Nanomaterials*, 2021, **11**, 1593.

74 R. W. Welker, in *Developments in Surface Contamination and Cleaning*, ed., R. Kohli and K. L. Mittal, William Andrew Publishing, Oxford, 2012, pp. 179–213, DOI: 10.1016/B978-1-4377-7883-0.00004-3.

75 Y.-M. Kim, J. Lee, D.-J. Jeon, S.-E. Oh and J.-S. Yeo, *Appl. Microsc.*, 2021, **51**, 7.

76 M. Lanza, U. Celano and F. Miao, *J. Electroceram.*, 2017, **39**, 94–108.

77 Y. Yang, X. Zhang, L. Qin, Q. Zeng, X. Qiu and R. Huang, *Nat. Commun.*, 2017, **8**, 15173.

78 M. Trapatseli, D. Carta, A. Regoutz, A. Khiat, A. Serb, I. Gupta and T. Prodromakis, *J. Phys. Chem. C*, 2015, **119**, 11958–11964.

79 Y. Sun, M. Tai, C. Song, Z. Wang, J. Yin, F. Li, H. Wu, F. Zeng, H. Lin and F. Pan, *J. Phys. Chem. C*, 2018, **122**, 6431–6436.

80 A. Mehonic, M. Buckwell, L. Montesi, M. S. Munde, D. Gao, S. Hudziak, R. J. Chater, S. Fearn, D. McPhail, M. Bosman, A. L. Shluger and A. J. Kenyon, *Adv. Mater.*, 2016, **28**, 7486–7493.

81 C. R. Peiris, S. Ferrie, S. Ciampi, W. D. A. Rickard and N. Darwish, *ACS Appl. Nano Mater.*, 2022, **5**, 6609–6617.

82 J.-Y. Mao, S. Wu, G. Ding, Z.-P. Wang, F.-S. Qian, J.-Q. Yang, Y. Zhou and S.-T. Han, *Small*, 2022, **18**, 2106253.

83 Z. Liu, P. Cheng, R. Kang, J. Zhou, X. Zhao, J. Zhao and Z. Zuo, *Adv. Mater. Interfaces*, 2023, **10**, 2201513.

84 R. A. John, N. Shah, S. K. Vishwanath, S. E. Ng, B. Febriansyah, M. Jagadeeswararao, C.-H. Chang, A. Basu and N. Mathews, *Nat. Commun.*, 2021, **12**, 3681.

85 L. Chen, Z.-Y. He, T.-Y. Wang, Y.-W. Dai, H. Zhu, Q.-Q. Sun and D. W. Zhang, *Electronics*, 2018, **7**, 80.

86 X. Guo, Q. Wang, X. Lv, H. Yang, K. Sun, D. Yang, H. Zhang, T. Hasegawa and D. He, *Nanoscale*, 2020, **12**, 4320–4327.

87 M. Patel, N. R. Hemanth, J. Gosai, R. Mohili, A. Solanki, M. Roy, B. Fang and N. K. Chaudhari, *Trends Chem.*, 2022, **4**, 835–849.

88 S. Ling, C. Zhang, C. Ma, Y. Li and Q. Zhang, *Adv. Funct. Mater.*, 2023, **33**, 2208320.

89 R. Xu, H. Jang, M.-H. Lee, D. Amanov, Y. Cho, H. Kim, S. Park, H.-J. Shin and D. Ham, *Nano Lett.*, 2019, **19**, 2411–2417.

90 X. Xiao, J. Hu, S. Tang, K. Yan, B. Gao, H. Chen and D. Zou, *Adv. Mater. Technol.*, 2020, **5**, 1900914.

91 X.-F. Cheng, W.-H. Qian, J. Wang, C. Yu, J.-H. He, H. Li, Q.-F. Xu, D.-Y. Chen, N.-J. Li and J.-M. Lu, *Small*, 2019, **15**, 1905731.

92 X. Wu, R. Ge, P.-A. Chen, H. Chou, Z. Zhang, Y. Zhang, S. Banerjee, M.-H. Chiang, J. C. Lee and D. Akinwande, *Adv. Mater.*, 2019, **31**, 1806790.

93 X. Shan, Z. Wang, Y. Lin, T. Zeng, X. Zhao, H. Xu and Y. Liu, *Adv. Electron. Mater.*, 2020, **6**, 2000536.

94 Y.-H. Ting, J.-Y. Chen, C.-W. Huang, T.-K. Huang, C.-Y. Hsieh and W.-W. Wu, *Small*, 2018, **14**, 1703153.

95 S. Pi, C. Li, H. Jiang, W. Xia, H. Xin, J. J. Yang and Q. Xia, *Nat. Nanotechnol.*, 2019, **14**, 35–39.

96 M. V. Il'ina, O. I. Il'in, Y. F. Blinov, V. A. Smirnov, A. S. Kolomiytsev, A. A. Fedotov, B. G. Konoplev and O. A. Ageev, *Carbon*, 2017, **123**, 514–524.

97 M. Lanza, R. Waser, D. Ielmini, J. J. Yang, L. Goux, J. Suñe, A. J. Kenyon, A. Mehonic, S. Spiga, V. Rana, S. Wiefels, S. Menzel, I. Valov, M. A. Villena, E. Miranda, X. Jing, F. Campabadal, M. B. Gonzalez, F. Aguirre, F. Palumbo, K. Zhu, J. B. Roldan, F. M. Puglisi, L. Larcher, T. H. Hou, T. Prodromakis, Y. Yang, P. Huang, T. Wan, Y. Chai, K. L. Pey, N. Raghavan, S. Dueñas, T. Wang, Q. Xia and S. Pazos, *ACS Nano*, 2021, **15**, 17214–17231.

98 A. Betal, J. Bera, A. Sharma, A. K. Rath and S. Sahu, *ACS Appl. Electron. Mater.*, 2022, **4**, 1109–1116.

99 T. Y. Wang, J. L. Meng, Q. X. Li, Z. Y. He, H. Zhu, L. Ji, Q. Q. Sun, L. Chen and D. W. Zhang, *Nano Energy*, 2021, **89**, 106291.

100 Y. C. Yang, F. Pan, Q. Liu, M. Liu and F. Zeng, *Nano Lett.*, 2009, **9**, 1636–1643.

101 J. J. Yang, M. X. Zhang, J. P. Strachan, F. Miao, M. D. Pickett, R. D. Kelley, G. Medeiros-Ribeiro and R. S. Williams, *Appl. Phys. Lett.*, 2010, **97**, 232102.

102 S. Wiefels, M. V. Witzleben, M. Hüttemann, U. Böttger, R. Waser and S. Menzel, *IEEE Trans. Electron Devices*, 2021, **68**, 1024–1030.

103 S. Goswami, A. J. Matula, S. P. Rath, S. Hedström, S. Saha, M. Annamalai, D. Sengupta, A. Patra, S. Ghosh, H. Jani, S. Sarkar, M. R. Motapothula, C. A. Nijhuis, J. Martin, S. Goswami, V. S. Batista and T. Venkatesan, *Nat. Mater.*, 2017, **16**, 1216–1224.

104 S. Boyn, S. Girod, V. Garcia, S. Fusil, S. Xavier, C. Deranlot, H. Yamada, C. Carrétéro, E. Jacquet, M. Bibes, A. Barthélémy and J. Grollier, *Appl. Phys. Lett.*, 2014, **104**, 052909.

105 E. J. Merced-Grafals, N. Dávila, N. Ge, R. S. Williams and J. P. Strachan, *Nanotechnology*, 2016, **27**, 365202.

106 R. Midya, Z. Wang, J. Zhang, S. E. Savel'ev, C. Li, M. Rao, M. H. Jang, S. Joshi, H. Jiang, P. Lin, K. Norris, N. Ge, Q. Wu, M. Barnell, Z. Li, H. L. Xin, R. S. Williams, Q. Xia and J. J. Yang, *Adv. Mater.*, 2017, **29**, 1604457.

107 K.-H. Kim, S. Hyun Jo, S. Gaba and W. Lu, *Appl. Phys. Lett.*, 2010, **96**, 053106.

108 T. Hussain, H. Abbas, C. Youn, H. Lee, T. Boynazarov, B. Ku, Y.-R. Jeon, H. Han, J. H. Lee, C. Choi and T. Choi, *Adv. Mater. Technol.*, 2022, **7**, 2100744.

© 2023 The Author(s). Published by the Royal Society of Chemistry

Open Access Article. Published on 31 ožujka 2023. Downloaded on 8.8.2024. 13:17:39.
This article is licensed under a Creative Commons Attribution-NonCommercial 3.0 Unported Licence.

109 Q. Gao, J. Huang, J. Gao, X. Geng, Y. Ji, H. Li, G. Wang, B. Liang, M. Wang, Z. Xiao, Y. Zhu, P. K. Chu and A. Huang, *Mater. Today Phys.*, 2023, **30**, 100947.
110 H. Li, S. Geng, T. Liu, M. Cao and J. Su, *ACS Appl. Mater. Interfaces*, 2023, **15**, 5456–5465.
111 P. Robin, T. Emmerich, A. Ismail, A. Niguès, Y. You, G. H. Nam, A. Keerthi, A. Siria, A. K. Geim, B. Radha and L. Bocquet, *Science*, 2023, **379**, 161–167.
112 Sudheer, R. Mandal, D. Hasina, A. Dutta, S. Alam Mollick, A. Mandal and T. Som, *Appl. Surf. Sci.*, 2023, **610**, 155411.
113 J. Guo, L. Liu, B. Bian, J. Wang, X. Zhao, Y. Zhang and Y. Yan, *Adv. Funct. Mater.*, 2023, 2212666.
114 A. K. Jena, M. C. Sahu, K. U. Mohanan, S. K. Mallik, S. Sahoo, G. K. Pradhan and S. Sahoo, *ACS Appl. Mater. Interfaces*, 2023, **15**, 3574–3585.
115 K. Rogdakis, M. Loizos, G. Viskadouros and E. Kymakis, *Mater. Adv.*, 2022, **3**, 7002–7014.
116 K. J. Kwak, J. H. Baek, D. E. Lee, I. H. Im, J. Kim, S. J. Kim, Y. J. Lee, J. Y. Kim and H. W. Jang, *Nano Lett.*, 2022, **22**, 6010–6017.
117 D. Li, B. Wu, X. Zhu, J. Wang, B. Ryu, W. D. Lu, W. Lu and X. Liang, *ACS Nano*, 2018, **12**, 9240–9252.
118 C. Li, M. Hu, Y. Li, H. Jiang, N. Ge, E. Montgomery, J. Zhang, W. Song, N. Dávila, C. E. Graves, Z. Li, J. P. Strachan, P. Lin, Z. Wang, M. Barnell, Q. Wu, R. S. Williams, J. J. Yang and Q. Xia, *Nat. Electron.*, 2018, **1**, 52–59.
119 P. M. Sheridan, F. Cai, C. Du, W. Ma, Z. Zhang and W. D. Lu, *Nat. Nanotechnol.*, 2017, **12**, 784–789.
120 S. Choi, J. H. Shin, J. Lee, P. Sheridan and W. D. Lu, *Nano Lett.*, 2017, **17**, 3113–3118.
121 M. Hu, C. E. Graves, C. Li, Y. Li, N. Ge, E. Montgomery, N. Davila, H. Jiang, R. S. Williams, J. J. Yang, Q. Xia and J. P. Strachan, *Adv. Mater.*, 2018, **30**, 1705914.
122 P. Lin, C. Li, Z. Wang, Y. Li, H. Jiang, W. Song, M. Rao, Y. Zhuo, N. K. Upadhyay, M. Barnell, Q. Wu, J. J. Yang and Q. Xia, *Nat. Electron.*, 2020, **3**, 225–232.
123 F. Cai, S. Kumar, T. Van Vaerenbergh, X. Sheng, R. Liu, C. Li, Z. Liu, M. Foltin, S. Yu, Q. Xia, J. J. Yang, R. Beausoleil, W. D. Lu and J. P. Strachan, *Nat. Electron.*, 2020, **3**, 409–418.
124 F. M. Bayat, M. Prezioso, B. Chakrabarti, H. Nili, I. Kataeva and D. Strukov, *Nat. Commun.*, 2018, **9**, 2331.
125 H. Kim, M. R. Mahmoodi, H. Nili and D. B. Strukov, *Nat. Commun.*, 2021, **12**, 1–11.
126 Q. Xia and J. J. Yang, *Nat. Mater.*, 2019, **18**, 309–323.
127 M. Prezioso, F. Merrikh-Bayat, B. D. Hoskins, G. C. Adam, K. K. Likharev and D. B. Strukov, *Nature*, 2015, **521**, 61–64.
128 C. H. Bennett, D. Garland, R. B. Jacobs-Gedrim, S. Agarwal and M. J. Marinella, Wafer-Scale TaOx Device Variability and Implications for Neuromorphic Computing Applications, *2019 IEEE International Reliability Physics Symposium (IRPS)*, Monterey, CA, USA, 2019, pp. 1–4, DOI: 10.1109/IRPS.2019.8720596.
129 R. B. Jacobs-Gedrim, D. R. Hughart, S. Agarwal, G. Vizkelethy, E. S. Bielejec, B. L. Vaandrager, S. E. Swanson, K. E. Knisely, J. L. Taggart, H. J. Barnaby and M. J. Marinella, *IEEE Trans. Nucl. Sci.*, 2019, **66**, 54–60.
130 F. Zeng, Y. Guo, W. Hu, Y. Tan, X. Zhang, J. Feng and X. Tang, *ACS Appl. Mater. Interfaces*, 2020, **12**, 23094–23101.
131 W. Zhang, L. Pan, X. Yan, G. Zhao, H. Chen, X. Wang, B. K. Tay, G. Zhong, J. Li and M. Huang, *Adv. Intell. Syst.*, 2021, **3**, 2100041.
132 Y. Wang, W. Wang, C. Zhang, H. Kan, W. Yue, J. Pang, S. Gao and Y. Li, *ACS Appl. Electron. Mater.*, 2022, **4**, 3525–3534.
133 Y. Guo, W. Hu, C. Zhang, Y. Peng and Y. Guo, *J. Phys. D: Appl. Phys.*, 2020, **53**, 195101.
134 Y. He, X. Zhong, J. Hu, D. Hou, Z. Zhang, D. Zeng and T. Shi, *Corros. Sci.*, 2020, **175**, 108880.
135 H. Herrera Hernández, F. González Díaz, G. D. J. Fajardo San Miguel, J. C. Velázquez Altamirano, C. O. González Morán and J. Morales Hernández, *Arabian J. Sci. Eng.*, 2019, **44**, 10087–10103.
136 S. Anantharaj and S. Noda, *ChemElectroChem*, 2020, **7**, 2297–2308.
137 Z. Cui, X. Liang, P. Wang, P. Zhou, Q. Zhang, Z. Wang, Z. Zheng, Y. Liu, Y. Dai and B. Huang, *Electrochim. Acta*, 2021, **395**, 139218.
138 Y. Zhang, F. Lian, J. Lu, L. Ma, N. Chen, Y. Chen and D. Xia, *J. Energy Chem.*, 2020, **46**, 144–151.
139 Y. Zhang, C. S. Kim, H. W. Song, S.-J. Chang, H. Kim, J. Park, S. Hu, K. Zhao and S. Lee, *Energy Storage Mater.*, 2022, **48**, 1–11.
140 A. Zaffora, D.-Y. Cho, K.-S. Lee, F. Di Quarto, R. Waser, M. Santamaria and I. Valov, *Adv. Mater.*, 2017, **29**, 1703357.
141 T. Tsuruoka, I. Valov, C. Mannequin, T. Hasegawa, R. Waser and M. Aono, *Jpn. J. Appl. Phys.*, 2016, **55**, 06GJ09.
142 S. Tappertzhofen, S. Menzel, I. Valov and R. Waser, *Appl. Phys. Lett.*, 2011, **99**, 203103.
143 S. Tappertzhofen, H. Mündelein, I. Valov and R. Waser, *Nanoscale*, 2012, **4**, 3040–3043.
144 M. Berruet, J. C. Pérez-Martínez, B. Romero, C. Gonzales, A. M. Al-Mayouf, A. Guerrero and J. Bisquert, *ACS Energy Lett.*, 2022, **7**, 1214–1222.
145 M. Lübben and I. Valov, *Adv. Electron. Mater.*, 2019, **5**, 1–8.
146 S. Tappertzhofen, R. Waser and I. Valov, *ChemElectroChem*, 2014, **1**, 1287–1292.
147 A. Mehonic, A. L. Shluger, D. Gao, I. Valov, E. Miranda, D. Ielmini, A. Bricalli, E. Ambrosi, C. Li, J. J. Yang, Q. Xia and A. J. Kenyon, *Adv. Mater.*, 2018, **30**, 1–21.
148 M. M. Mogadem and Y. Li, *Sustainability*, 2021, **13**, 11204.
149 C. C. Lin, J. F. Tang, H. H. Su, C. S. Hong, C. Y. Huang and S. Y. Chu, *J. Appl. Phys.*, 2016, **119**, 1–7.
150 C. S. Dash, S. Sahoo and S. R. S. Prabaharan, *Solid State Ionics*, 2018, **324**, 218–225.
151 M. Zhao, B. Gao, Y. Xi, F. Xu, H. Wu and H. Qian, *IEEE J. Electron Devices Soc.*, 2019, **7**, 1239–1247.
152 B. Chen, Y. Lu, B. Gao, Y. H. Fu, F. F. Zhang, P. Huang, Y. S. Chen, L. F. Liu, X. Y. Liu, J. F. Kang, Y. Y. Wang, Z. Fang, H. Y. Yu, X. Li, X. P. Wang, N. Singh, G. Q. Lo and D. L. Kwong, Technical Digest - International Electron

Open Access Article. Published on 31 ožujka 2023. Downloaded on 8.8.2024. 13:17:39.
This article is licensed under a Creative Commons Attribution-NonCommercial 3.0 Unported Licence.

Devices Meeting, *IEDM*, 2011, 283–286, DOI: 10.1109/IEDM.2011.6131539.
153 A. V. Fadeev and K. V. Rudenko, *Russ. Microelectron.*, 2021, **50**, 311–325.
154 M. Tu, H. Lu, S. Luo, H. Peng, S. Li, Y. Ke, S. Yuan, W. Huang, W. Jie and J. Hao, *ACS Appl. Mater. Interfaces*, 2020, **12**, 24133–24140.
155 K. M. Kim, J. J. Yang, J. P. Strachan, E. M. Grafals, N. Ge, N. D. Melendez, Z. Li and R. S. Williams, *Sci. Rep.*, 2016, **6**, 1–6.
156 M. J. Lee, C. B. Lee, D. Lee, S. R. Lee, M. Chang, J. H. Hur, Y. B. Kim, C. J. Kim, D. H. Seo, S. Seo, U. I. Chung, I. K. Yoo and K. Kim, *Nat. Mater.*, 2011, **10**, 625–630.
157 M. Ismail, I. Talib, A. M. Rana, E. Ahmed and M. Y. Nadeem, *J. Appl. Phys.*, 2015, **117**, 084502.
158 M. Zhao, H. Wu, B. Gao, X. Sun, Y. Liu, P. Yao, Y. Xi, X. Li, Q. Zhang, K. Wang, S. Yu and H. Qian, *2018 IEEE International Electron Devices Meeting (IEDM)*, San Francisco, CA, USA, 2018, pp. 20.2.1–20.2.4, DOI: 10.1109/IEDM.2018.8614664.
159 C. Y. Chen, L. Goux, A. Fantini, S. Clima, R. Degraeve, A. Redolfi, Y. Y. Chen, G. Groeseneken and M. Jurczak, *Appl. Phys. Lett.*, 2015, **106**, 053501.
160 H. Lv, X. Xu, H. Liu, R. Liu, Q. Liu, W. Banerjee, H. Sun, S. Long, L. Li and M. Liu, *Sci. Rep.*, 2015, **5**, 1–6.
161 W. Zhang, J.-Z. Kong, Z.-Y. Cao, A.-D. Li, L.-G. Wang, L. Zhu, X. Li, Y.-Q. Cao and D. Wu, *Nanoscale Res. Lett.*, 2017, **12**, 393.
162 J.-H. Lee, J.-M. Yang, S.-Y. Kim, S. Baek, S. Lee, S.-J. Lee, N.-G. Park and J.-W. Lee, *Adv. Funct. Mater.*, 2023, 2214142.
163 S. Kumar, Z. Wang, X. Huang, N. Kumari, N. Davila, J. P. Strachan, D. Vine, A. L. D. Kilcoyne, Y. Nishi and R. S. Williams, *Appl. Phys. Lett.*, 2017, **110**, 103503.
164 S. Fujii, J. A. C. Incorvia, F. Yuan, S. Qin, F. Hui, Y. Shi, Y. Chai, M. Lanza and H. S. P. Wong, *IEEE Electron Device Lett.*, 2018, **39**, 23–26.
165 S. Kumar, M. Das, M. T. Htay, S. Sriram and S. Mukherjee, *ACS Appl. Electron. Mater.*, 2022, **4**, 3080–3087.
166 S. Yarragolla, N. Du, T. Hemke, X. Zhao, Z. Chen, I. Polian and T. Mussenbrock, *Sci. Rep.*, 2022, **12**, 20490.
167 F. Zahoor, T. Z. Azni Zulkifli and F. A. Khanday, *Nanoscale Res. Lett.*, 2020, **15**, 90.
168 A. M. Rana, T. Akbar, M. Ismail, E. Ahmad, F. Hussain, I. Talib, M. Imran, K. Mehmood, K. Iqbal and M. Y. Nadeem, *Sci. Rep.*, 2017, **7**, 1–15.
169 L. Zhang, Z. Xu, J. Han, L. Liu, C. Ye, Y. Zhou, W. Xiong, Y. Liu and G. He, *J. Mater. Sci. Technol.*, 2020, **49**, 1–6.
170 W. Tian, N. Ilyas, D. Li, C. Li, X. Jiang and W. Li, *J. Phys.: Conf. Ser.*, 2020, **1637**, 3–8.
171 Z. Ma, J. Ge, W. Chen, X. Cao, S. Diao, Z. Liu and S. Pan, *ACS Appl. Mater. Interfaces*, 2022, **14**, 21207–21216.
172 S. S. Zumdahl, S. A. Zumdahl and D. J. DeCoste, *Chemistry*, Cengage Learning, 2016.
173 Z. Wang, W. Xiao, H. Yang, S. Zhang, Y. Zhang, K. Sun, T. Wang, Y. Fu, Q. Wang, J. Zhang, T. Hasegawa and D. He, *ACS Appl. Mater. Interfaces*, 2022, **14**, 1557–1567.
174 X. Zhao, J. Ma, X. Xiao, Q. Liu, L. Shao, D. Chen, S. Liu, J. Niu, X. Zhang, Y. Wang, R. Cao, W. Wang, Z. Di, H. Lv, S. Long and M. Liu, *Adv. Mater.*, 2018, **30**, 1705193.
175 B. K. You, J. M. Kim, D. J. Joe, K. Yang, Y. Shin, Y. S. Jung and K. J. Lee, *ACS Nano*, 2016, **10**, 9478–9488.
176 B. K. You, W. I. Park, J. M. Kim, K.-I. Park, H. K. Seo, J. Y. Lee, Y. S. Jung and K. J. Lee, *ACS Nano*, 2014, **8**, 9492–9502.
177 L. Jiang, Y. Jin, Y. Zhao, J. Meng, J. Zhang, X. Chen, X. Wu, Y. Xiao, Z. Tao, B. Jiang, X. Wen and C. Ye, *Adv. Phys. Res.*, 2023, 2200086.
178 H. Wu, X. Li, M. Wu, F. Huang, Z. Yu and H. Qian, *IEEE Electron Device Lett.*, 2014, **35**, 39–41.
179 J. Liu, H. Yang, Z. Ma, K. Chen, X. Zhang, X. Huang and S. Oda, *J. Phys. D: Appl. Phys.*, 2018, **51**, 025102.
180 R. Nakamura, T. Toda, S. Tsukui, M. Tane, M. Ishimaru, T. Suzuki and H. Nakajima, *J. Appl. Phys.*, 2014, **116**, 033504.
181 Y. Shuai, N. Du, X. Ou, W. Luo, S. Zhou, O. G. Schmidt and H. Schmidt, *Phys. Status Solidi C*, 2013, **10**, 636–639.
182 J. H. Sung, J. H. Park, D. S. Jeon, D. Kim, M. J. Yu, A. C. Khot, T. D. Dongale and T. G. Kim, *Mater. Des.*, 2021, **207**, 109845.
183 J. Park, J. Choi, G. Kim, G. Kim, G. S. Kim, H. Song, Y. S. Kim, Y. Lee, H. Rhee, H. M. Lee, C. S. Hwang and K. M. Kim, *ACS Appl. Mater. Interfaces*, 2022, **14**, 35949–35958.
184 T. Guo, K. Pan, Y. Jiao, B. Sun, C. Du, J. P. Mills, Z. Chen, X. Zhao, L. Wei, Y. N. Zhou and Y. A. Wu, *Nanoscale Horiz.*, 2022, **7**, 299–310.
185 Y. Wang, Y. Gong, L. Yang, Z. Xiong, Z. Lv, X. Xing, Y. Zhou, B. Zhang, C. Su, Q. Liao and S. T. Han, *Adv. Funct. Mater.*, 2021, **31**, 1–10.
186 V. Q. Le, T. H. Do, J. R. D. Retamal, P. W. Shao, Y. H. Lai, W. W. Wu, J. H. He, Y. L. Chueh and Y. H. Chu, *Nano Energy*, 2019, **56**, 322–329.
187 G. Zhou, B. Sun, X. Hu, L. Sun, Z. Zou, B. Xiao, W. Qiu, B. Wu, J. Li, J. Han, L. Liao, C. Xu, G. Xiao, L. Xiao, J. Cheng, S. Zheng, L. Wang, Q. Song and S. Duan, *Adv. Sci.*, 2021, **8**, 2003765.
188 T. Wang, Z. Cui, Y. Liu, D. Lu, M. Wang, C. Wan, W. R. Leow, C. Wang, L. Pan, X. Cao, Y. Huang, Z. Liu, A. I. Y. Tok and X. Chen, *Adv. Mater.*, 2022, **34**, 2106212.
189 Y. Song, X. Wang, Q. Wu, C. Wang, S. Du, L. Zhang and X. Miao, *Appl. Phys. Lett.*, 2021, **118**, 223501.
190 W. Wang, S. Liu, Q. Li, T. Shi, F. Zhang, H. Liu, N. Li, Y. Wang, Y. Sun, B. Song, H. Xu and Q. Liu, *Adv. Intell. Syst.*, 2022, **4**, 2200207.
191 I. H. Im, S. J. Kim, J. H. Baek, K. J. Kwak, T. H. Lee, J. W. Yang, D. E. Lee, J. Y. Kim, H. R. Kwon, D. Y. Heo, S. Y. Kim and H. W. Jang, *Adv. Funct. Mater.*, 2022, 2211358.
192 W. Wang, M. Laudato, E. Ambrosi, A. Bricalli, E. Covi, Y. H. Lin and D. Ielmini, *IEEE Trans. Electron Devices*, 2019, **66**, 3795–3801.
193 W. Wang, M. Laudato, E. Ambrosi, A. Bricalli, E. Covi, Y. H. Lin and D. Ielmini, *IEEE Trans. Electron Devices*, 2019, **66**, 3802–3808.
194 C.-P. Hsiung, H.-W. Liao, J.-Y. Gan, T.-B. Wu, J.-C. Hwang, F. Chen and M.-J. Tsai, *ACS Nano*, 2010, **4**, 5414–5420.

© 2023 The Author(s). Published by the Royal Society of Chemistry

Open Access Article. Published on 31 ožujka 2023. Downloaded on 8.8.2024. 13:17:39.
This article is licensed under a Creative Commons Attribution-NonCommercial 3.0 Unported Licence.

195 W. Wang, M. Wang, E. Ambrosi, A. Bricalli, M. Laudato, Z. Sun, X. Chen and D. Ielmini, *Nat. Commun.*, 2019, **10**, 81.

196 C. Wang, G.-Q. Mao, M. Huang, E. Huang, Z. Zhang, J. Yuan, W. Cheng, K.-H. Xue, X. Wang and X. Miao, *Adv. Sci.*, 2022, **9**, 2201446.

197 Z. Hu, F. Cao, T. Yan, L. Su and X. Fang, *J. Mater. Chem. C*, 2023, **11**, 244–251.

198 J. Fu, Z. Liao and J. Wang, *IEEE Trans. Very Large Scale Integr. Syst.*, 2019, **27**, 2745–2754.

199 Z. Wang, H. Wu, G. W. Burr, C. S. Hwang, K. L. Wang, Q. Xia and J. J. Yang, *Nat. Rev. Mater.*, 2020, **5**, 173–195.

200 J. Zhu, T. Zhang, Y. Yang and R. Huang, *Appl. Phys. Rev.*, 2020, **7**, 1–107.

201 T. Hasegawa, T. Ohno, K. Terabe, T. Tsuruoka, T. Nakayama, J. K. Gimzewski and M. Aono, *Adv. Mater.*, 2010, **22**, 1831–1834.

202 S. Kim, S. Choi and W. Lu, *ACS Nano*, 2014, **8**, 2369–2376.

203 Y. Jeong, S. Kim and W. D. Lu, *Appl. Phys. Lett.*, 2015, **107**, 173105.

204 S. Larentis, F. Nardi, S. Balatti, D. C. Gilmer and D. Ielmini, *IEEE Trans. Electron Devices*, 2012, **59**, 2468–2475.

205 Y. Jiang, K. Zhang, K. Hu, Y. Zhang, A. Liang, Z. Song, S. Song and F. Wang, *Mater. Sci. Semicond. Process.*, 2021, **136**, 106131.

206 S.-M. Park, H.-G. Hwang, J.-U. Woo, W.-H. Lee, S.-J. Chae and S. Nahm, *ACS Appl. Mater. Interfaces*, 2020, **12**, 1069–1077.

207 J.-U. Woo, H.-G. Hwang, S.-M. Park, T.-G. Lee and S. Nahm, *Appl. Mater. Today*, 2020, **19**, 100582.

208 S. Chandrasekaran, F. M. Simanjuntak, R. Saminathan, D. Panda and T.-Y. Tseng, *Nanotechnology*, 2019, **30**, 445205.

209 J. Kang, T. Kim, S. Hu, J. Kim, J. Y. Kwak, J. Park, J. K. Park, I. Kim, S. Lee, S. Kim and Y. Jeong, *Nat. Commun.*, 2022, **13**, 4040.

210 H. Yeon, P. Lin, C. Choi, S. H. Tan, Y. Park, D. Lee, J. Lee, F. Xu, B. Gao, H. Wu, H. Qian, Y. Nie, S. Kim and J. Kim, *Nat. Nanotechnol.*, 2020, **15**, 574–579.

211 Z. Y. Shao, H. M. Huang and X. Guo, *Solid State Ionics*, 2021, **370**, 115746.

212 S. Chandrasekaran, F. M. Simanjuntak, D. Panda and T. Y. Tseng, *IEEE Trans. Electron Devices*, 2019, **66**, 4722–4726.

213 J.-Y. Tsai, J. Pan, H. Lin, A. Bansil and Q. Yan, *Nat. Commun.*, 2022, **13**, 492.

214 J. P. Perdew, S. T. u R. Chowdhury, C. Shahi, A. D. Kaplan, D. Song and E. J. Bylaska, *J. Phys. Chem. A*, 2023, **127**, 384–389.

215 S. Dasgupta, E. Lambros, J. P. Perdew and F. Paesani, *Nat. Commun.*, 2021, **12**, 6359.

216 P. K. Schelling, S. R. Phillpot and P. Keblinski, *Appl. Phys. Lett.*, 2002, **80**, 2484–2486.

217 S. Prada, M. Rosa, L. Giordano, C. Di Valentin and G. Pacchioni, *Phys. Rev. B: Condens. Matter Mater. Phys.*, 2011, **83**, 245314.

218 N. Onofrio and A. Strachan, *J. Chem. Phys.*, 2015, **143**, 054109.

219 S. Ambrogio, B. Magyari-Köpe, N. Onofrio, M. Mahbubul Islam, D. Duncan, Y. Nishi and A. Strachan, *J. Electroceram.*, 2017, **39**, 39–60.

220 G. Di Martino, A. Demetriadou, W. Li, D. Kos, B. Zhu, X. Wang, B. de Nijs, H. Wang, J. MacManus-Driscoll and J. J. Baumberg, *Nat. Electron.*, 2020, **3**, 687–693.

221 M. L. Urquiza, M. M. Islam, A. C. T. van Duin, X. Cartoixà and A. Strachan, *ACS Nano*, 2021, **15**, 12945–12954.

222 S.-G. Xu, P. Zhang and X. Zhang, *Phys. Rev. Mater.*, 2021, **5**, 024603.

223 L. Gao, Q. Ren, J. Sun, S.-T. Han and Y. Zhou, *J. Mater. Chem. C*, 2021, **9**, 16859–16884.

224 Y.-L. Zhu, K.-H. Xue, X.-M. Cheng, C. Qiao, J.-H. Yuan, L.-H. Li and X.-S. Miao, *Appl. Surf. Sci.*, 2021, **550**, 149274.

225 R. Goul, A. Marshall, S. Seacat, H. Peelaers, F. C. Robles Hernandez and J. Z. Wu, *Commun. Phys.*, 2022, **5**, 260.

226 N. Onofrio, D. Guzman and A. Strachan, *Nat. Mater.*, 2015, **14**, 440–446.

© 2023 The Author(s). Published by the Royal Society of Chemistry